Check for updates

Advanced Functional Materials

ADVANCED FUNCTIONAL MATERIALS
www.afm-journal.de

RESEARCH ARTICLE OPEN ACCESS

Exceptional Electro-Optic Coefficient Unlocked via Polarization Swaying in $KNbO_3$ Thin Films

Sankalpa Hazra[1] | Aiden Ross[1] | Brynn Brower[2] | Tobias Schwaigert[3,4] | Ian Reed Philippi[1] | Albert Suceava[1] | Himirkanti Sarkar[1] | Muhammed Aminul Haque Chowdhury[1] | Suchismita Sarker[5] | Darrell G. Schlom[5,6,7] | Long-Qing Chen[1,2] | Venkatraman Gopalan[1,2]

[1]Department of Materials Science and Engineering, The Pennsylvania State University, University Park, Pennsylvania, USA | [2]Department of Physics, The Pennsylvania State University, University Park, Pennsylvania, USA | [3]Platform for the Accelerated Realization, Analysis, and Discovery of Interface Materials (PARADIM), Cornell University, Ithaca, New York, USA | [4]Department of Materials Science and Engineering, Cornell University, Ithaca, New York, USA | [5]Cornell High Energy Synchrotron Source, Cornell University, Ithaca, New York, USA | [6]Kavli Institute at Cornell for Nanoscale Science, Ithaca, New York, USA | [7]Leibniz-Institut für Kristallzüchtung, Berlin, Germany

Correspondence: Venkatraman Gopalan (vgopalan@psu.edu)

Received: 14 July 2026 | **Revised:** 11 September 2026 | **Accepted:** 1 October 2026

Keywords: electro-optics | ferroelectric thin films | monoclinic symmetry | strain tuning

ABSTRACT

The electro-optic effect powers microwave-to-optical quantum transducers, photonic quantum computing switches, and high-speed optical interconnects. A larger electro-optic coefficient directly reduces the drive voltage and device footprint of electro-optic modulators, making the search for materials with large coefficients a central challenge in photonics. Here, guided by phase-field modeling, we engineer an electro-optic coefficient of 43 000 pm V^{-1} in monoclinic $KNbO_3$ thin films, the largest ever measured in any material, exceeding industry-standard $LiNbO_3$ by 1000×. This exceptional response arises from electric field-driven "lateral swaying" of the ferroelectric polarization vector between symmetry-equivalent monoclinic variants, which reorients the optical index ellipsoid far beyond the conventional Pockels response that relies on a linear coupling between field and polarization. The ultralow coercive fields of the monoclinic phase (~1 kV cm^{-1}) place this giant response within reach of standard drive electronics, enabling drive voltages orders of magnitude below the current state-of-the-art. The response is stable to within 1% − 2% over hours, robust under thermal and electrical cycling, and demonstrated up to 1 MHz, establishing low-symmetry ferroelectric phases as an unexploited design space for next-generation energy-efficient electro-optic modulators for classical and quantum photonic integrated circuits.

1 | Introduction

The electro-optic effect describes a change in the refractive index (n_{ij}) of a material in response to an applied electric field, E_K, given by, $\Delta\left(\frac{1}{n^2}\right)_{ij} = \Delta B_{ij} = r_{ijk}\ E_k$, where, $B_{ij} = \left(\frac{1}{n^2}\right)_{ij}$ is the optical dielectric stiffness tensor, r_{ijk} is the Pockels tensor, and the dummy subscripts indicate crystal physics axes [1]. Electro-optic modulators exploiting this effect are essential for modern photonic systems, enabling high-speed optical information transfer in applications ranging from optical interconnects in data centers [2] and LiDAR [3] to cryogenic photonic systems for quantum computing architectures [4]. A larger electro-optic coefficient reduces drive voltages and enables more compact photonic device geometries [5]. Lithium niobate ($LiNbO_3$) remains the

Sankalpa Hazra, Aiden Ross, and Brynn Brower contributed equally to this work.

This is an open access article under the terms of the Creative Commons Attribution License, which permits use, distribution and reproduction in any medium, provided the original work is properly cited.
© 2026 The Author(s). *Advanced Functional Materials* published by Wiley-VCH GmbH

industry benchmark [6], yet its modest electro-optic coefficient and limited compatibility with silicon photonics motivate the search for alternative materials. Ferroelectric perovskite oxides have emerged as promising candidates, offering large intrinsic electro-optic coefficients and compatibility with thin-film growth on silicon [5, 7].

A largely unexplored route to giant electro-optic responses lies in exploiting the shallow polarization energy landscape of low-symmetry ferroelectric phases [8]. In ferroelectrics, $\frac{\partial B}{\partial E} = \frac{\partial B}{\partial P}\frac{\partial P}{\partial E} = g\frac{\partial P}{\partial E}$, where the subscripts are suppressed for clarity. While the polar-optic tensor g is intrinsic, the $\frac{\partial P}{\partial E}$ can be extrinsically tuned to large values by appropriate phase and domain engineering. Here, we exploit the "swaying" degree of freedom of the ferroelectric polarization in low-symmetry phases, where the sideways motion of the polarization vector rotates the optical index ellipsoid, producing a change in refractive index that can far exceed the intrinsic Pockels response. While ferroelectric switching often involves large coercive fields which limit its practicality for low-voltage modulation, low-symmetry ferroelectric phases, however, harbor degenerate polarization variants separated by low energy barriers, enabling small coercive fields [9, 10]. In monoclinic $BaTiO_3$ [8], this swaying mechanism yields a cryogenic electro-optic response of $\sim$ 2500 pmV^{-1}. We demonstrate that a further order of magnitude enhancement in the switching-driven electro-optic coefficient is possible in monoclinic $KNbO_3$ where a larger polarization swaying is observed.

Here, we engineer a switching-driven electro-optic coefficient of $\sim$43 000 pm V^{-1} at 5 K by harnessing polarization swaying in strain-stabilized monoclinic $KNbO_3$ thin films. This represents the largest reported electro-optic coefficient in any material to date, exceeding $LiNbO_3$ [11] by 1000×, bulk $KNbO_3$ [12] by 100×, and monoclinic $BaTiO_3$ thin films [8] by 20×. Phase-field simulations quantitatively reproduce this giant switching-driven electro-optic response and identify its microscopic origin: electric field-driven polarization swaying between monoclinic variants, which induces associated reorientation of the optical index ellipsoid. The electro-optic response is stable within $1\% - 2\%$ over hours, is robust under thermal and electrical cycling, and remains stable at modulation frequencies up to at least 1 MHz, our current experimental capability. This establishes polarization swaying in low-symmetry ferroelectric phases as a new mechanism for giant electro-optic response enabling low-voltage electro-optic modulators for classical and quantum photonic integrated circuits.

2 | Monoclinic Phase in $KNbO_3$

In its bulk form, $KNbO_3$ undergoes a sequence of temperature-dependent structural phase transitions, from cubic to tetragonal at 676 K, tetragonal to orthorhombic at 498 K, and orthorhombic to rhombohedral at 223 K [13]. This phase transition sequence can be altered under a biaxial compressive epitaxial strain, $\varepsilon = (a_{||} - a_0)/a_0$, where a_0 is the effective cubic lattice parameter extrapolated from the high-temperature $KNbO_3$ cubic phase and $a_{||}$ is the in-plane lattice parameter of the $KNbO_3$ thin film constrained to the substrate. Under a compressive strain, the out-of-plane polarization direction is energetically favored, stabilizing a tetragonal phase (space group $P4mm$) at high temperatures that transitions into a monoclinic phase (space group Pm) upon cooling (Figure 1a). When $KNbO_3$ is grown on $GdScO_3$ ($\varepsilon = -1.1\%$) (Figure S1), this transition occurs at ~275 K [14].

Phase-field simulations identify the observed monoclinic phase as space group Pm, with unit cell polarization (P_x, 0, P_z) or (0, P_y, P_z), confined within the mirror plane perpendicular to {010}. This is distinct from the Cm monoclinic phase where polarization lies in the mirror plane perpendicular to the {110} diagonal. This has been previously confirmed by x-ray reciprocal space mapping [14]. Across the tetragonal-to-monoclinic transition, while the phase-field predicted P_z remains relatively temperature-independent, P_x becomes nonzero below 275 K (Figure 1b), marking the onset of the transition. Beyond the transition, P_x increases with decreasing temperature in the monoclinic phase. This is experimentally confirmed by normal-incidence second harmonic generation (SHG) (I_{SHG}) measurements (Figure S2 and Table S1), which is sensitive to P_x ($\sqrt{I_{SHG}} \propto P_x$) [15]. Normal incidence SHG signal is only observed below ~275 K (monoclinic phase), while vanishing in the tetragonal phase and increasing as the temperature is lowered. Temperature-dependent x-ray diffraction measurements further confirm the onset of the monoclinic phase below 275 K (Figure S3). Figure 1c shows the phase-field simulated temperature-strain phase diagram of $KNbO_3$ for the compressively strained regime, highlighting the relative phase stability regimes of the tetragonal and monoclinic phases.

The monoclinic phase gives rise to symmetry-equivalent variants that differ only in their in-plane polarization component. For example, two monoclinic variants can exist with P_x along [100] and [$\bar{1}$00], both with identical P_z, separated by a shallow energy barrier (Figure 1a). Under an in-plane electric field E_x, P_x switches from left to right while leaving the P_z component unchanged; this polarization dynamics is dubbed here as "swaying" because the net polarization vector effectively swings from left to right while being confined within the monoclinic mirror plane. This swaying reorients the optical index ellipsoid in the laboratory reference frame (x, y, z), giving rise to a large change in the refractive index experienced by a probe beam.

To confirm such an electric field-driven in-plane polarization switching in the monoclinic phase, SHG hysteresis loops were measured under an applied in-plane electric field (E_{DC}). Figure 1d shows a two-step hysteresis loop of $\sqrt{I_{SHG}}$ vs. E_{DC} normalized by the coercive field (E_c), compared with phase-field simulated switching of P_x. While the qualitative agreement is excellent, the magnitude of E_c is ~1 kV cm^{-1} for experiments and ~ 30 kV cm^{-1} for simulations. Such an overestimation of coercive fields in phase-field simulations is well known [16–18], and is related to extrinsic vs. intrinsic factors at play. While the maximum slope of the energy barrier within a double-well potential determines the intrinsic E_c, the inclusion of extrinsic factors such as defect-mediated nucleation, increased system size for simulation, and varying the field ramp rate can bring the predicted coercive field closer to the experiments.

Next, we discuss the electro-optic response. Figure 1e depicts the phase-field simulated index ellipsoid of the monoclinic phase at 5 K. An oblique incident probe beam experiences two

16163028, 0, Downloaded from https://advanced.onlinelibrary.wiley.com/doi/10.1002/adfm.79070, Wiley Online Library on [16/11/2026]. See the Terms and Conditions (https://onlinelibrary.wiley.com/terms-and-conditions) on Wiley Online Library for rules of use; OA articles are governed by the applicable Creative Commons License

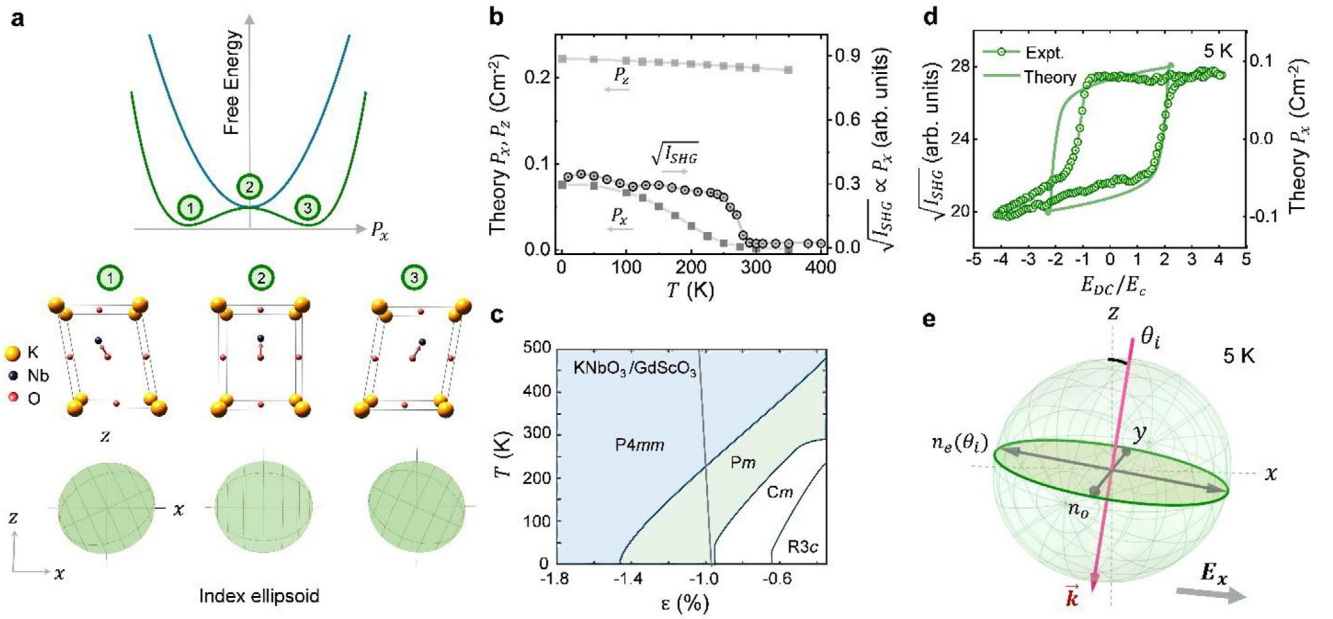


FIGURE 1 | (a) Schematic free-energy landscape as a function of the in-plane polarization component, P_x, for the tetragonal phase (space group $P4mm$) with a single minimum at $P_x = 0$, and the two monoclinic variants (space group Pm) with minima at $\pm P_x$. A schematic of the polarization swaying pathway in the monoclinic unit cell from state 1 (left) to state 3 (right) through state 2 (middle), along with the associated index ellipsoid reorientation, is shown below. The monoclinic unit cell sheer and the index ellipsoid reorientation are exaggerated for clarity. (b) Phase-field simulated polarization components P_z and P_x as a function of temperature, compared to the square root of the second-harmonic generation (SHG) intensity measured at normal incidence ($\sqrt{I_{SHG}} \propto P_x$). A non-zero SHG response below 275 K marks the tetragonal-to-monoclinic phase transition. (c) Phase-field predicted temperature–strain phase diagram for $KNbO_3$, showing the stability region of the monoclinic phase under biaxial compressive strain. (d) $\sqrt{I_{SHG}}$ as a function of the DC in-plane electric field applied (E_{DC}) normalized by the coercive field (E_C), E_{DC}/E_C at 5 K, showing a hysteretic loop consistent with the phase-field predicted switching loop of P_x. E_C is 1 kV cm^{-1} for experiments and 30 kV cm^{-1} for phase-field. (e) Phase-field simulated optical index ellipsoid of a monoclinic unit cell (state 3) at 5 K showing the probe beam geometry, beam propagation direction, and the measured refractive indices.

orthogonal refractive indices, $n_e(\theta_{film})$ and n_o, where $n_e(\theta_{film})$ is the extraordinary refractive index for an incidence angle θ_{film} inside the film and n_o is the ordinary refractive index. Under an applied in-plane electric field, E_x, the index ellipsoid reorients between the two monoclinic variants, as shown in Video S1. The probe beam now experiences new refractive indices, $n_e'(\theta_{film})$ and $n_o' = n_o$ (Figure S4). The resultant Δn ($= n_e(\theta_{film}) - n_e'(\theta_{film})$) is measured using a standardized polarizer-sample-compensator-analyzer (PSCA) setup with an oblique incident probe beam [8, 19, 20] (Figures S5 and S6). Here, the change in light transmission through a pair of crossed polarizers is measured as a function of an applied electric field to evaluate the change in the refractive indices of the sample [21–29, 20, 30]. To ensure accurate extraction of electro-optic coefficients, the setup is tested against a single-crystal $LiNbO_3$ reference sample (Figure S7).

3 | Giant Electro-Optic Response in $KNbO_3$ on $GdScO_3$

Figure 2a depicts the experimentally measured Δn as a function of an applied AC electric field amplitude (E_{AC}) normalized by E_C (Figure 1c) at 555 Hz measured on a 20 nm thin $KNbO_3$ film grown on $GdScO_3$. In the tetragonal phase (400 K), where the polarization is oriented fully out-of-plane, Δn varies linearly with the applied in-plane electric field, consistent with the conventional Pockels response [19]. In contrast, in the monoclinic phase (5 K), the in-plane electric field drives a sharp step-like change in Δn. As the temperature increases, this sharp step-like change in Δn vs. E_{AC}/E_C smoothens, eventually becoming linear in the tetragonal phase (Figure S8). This behavior is also captured by phase-field simulations, which are converted to Δn vs. E_{AC}/E_C curves based on the experimental geometry used and accounting for a lock-in detection scheme. This is further elaborated in the Supporting Information.

To extract the effective electro-optic coefficients from this multi-regime response at 5 K (Figure 2b), the slopes of the Δn vs. E_{AC}/E_C curves are taken in three regimes: the low-field linear regime ($E_{AC}/E_C < 1$), the switching regime ($1.2 < E_{AC}/E_C < 1.5$), and the high-field linear regime ($E_{AC}/E_C > 3$). This yields three effective electro-optic coefficients, r_{lf}, r_{max}, and r_{hf} (see Supporting Information). Temperature-dependent zero-field refractive indices necessary for quantifying electro-optic coefficients are measured from spectroscopic ellipsometry and are shown in Figures S9–S11 and Tables S2,S3.

The experimentally measured and phase-field simulated r_{lf} (Figure 2c) as a function of temperature reveals that both coefficients peak to a value of ~ 1000 pm V^{-1} near the tetragonal-to-monoclinic phase transition and reaching ~ 300 pm V^{-1} away from the transition. The linear electro-optic coefficients, r_{lf} and r_{hf}, are comparable in magnitude across the entire temperature range and indicate that the two monoclinic variants before and after the swaying possess similar electro-optic responses, as shown in Figure S12.

16163028, 0, Downloaded from https://advanced.onlinelibrary.wiley.com/doi/10.1002/adfm.79070, Wiley Online Library on [16/11/2026]. See the Terms and Conditions (https://onlinelibrary.wiley.com/terms-and-conditions) on Wiley Online Library for rules of use; OA articles are governed by the applicable Creative Commons License

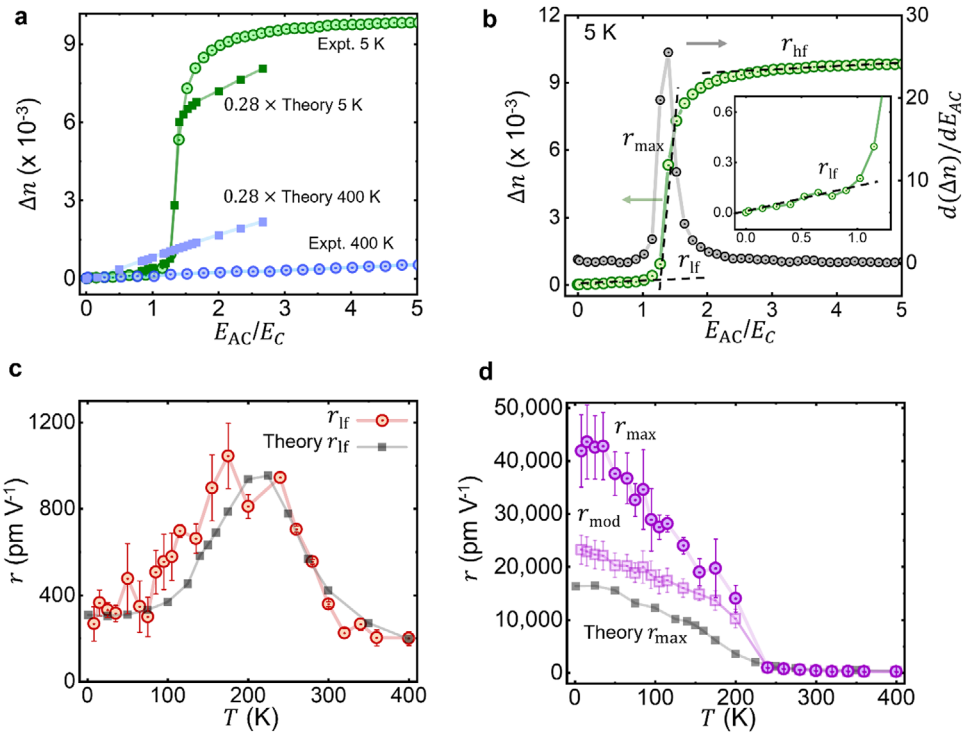


FIGURE 2 | (a) Experimentally measured change in refractive index, Δn ($= \Delta(n_e(\theta_{film}) - n_e'(\theta_{film}))$ as a function of E_{AC}/E_C at 555 Hz compared to phase-field simulations. E_C is 1 kV cm^{-1} for experiments and 30 kV cm^{-1} for phase-field. In the tetragonal phase (400 K), Δn varies linearly with E_{AC}, while in the monoclinic phase a multi-regime response emerges with a large Δn change at the switching field. (b) Δn vs. E_{AC}/E_C at 5 K showing the three distinct regimes: low-field linear (r_{lf}), switching field (r_{max}), and high-field linear (r_{hf}), with the corresponding slopes indicated. The derivative $d\Delta n/dE_{AC}$ is also shown, highlighting the peak at the switching field corresponding to r_{max}. A zoomed-in low-field regime of the curve is shown in the inset. (c) Temperature dependence of the experimentally measured r_{lf} alongside phase-field simulations at low field, showing a peak near the tetragonal-to-monoclinic transition temperature reaching ~1100 pm V^{-1}. (d) Temperature dependence of the experimentally measured r_{max} and r_{mod} alongside phase-field simulations. r_{max} is calculated from the slope of the Δn vs. E_{AC} curves within a window of 0.5 kV cm^{-1} around the inflection point, while r_{mod} is extracted using a finite AC amplitude window of 1.25 kV cm^{-1} centered around the inflection point of the curve. Both show a large enhancement below the transition temperature, with r_{max} reaching 43 000 pm V^{-1} and r_{mod} reaching 23 000 pm V^{-1} at 5 K.

In an oblique incident probe geometry, the experimentally observed electro-optic response is dominated by the r_{131} (r_{51} in Voigt notation) electro-optic tensor coefficient, as dictated by the monoclinic phase (point group m) and the experimental geometry (Figures S13 and S14). In our experiments, the sample is oriented so the crystal physics directions (1, 2, 3) coincide with the lab coordinates (x, y, z) (see Supporting Information). In the crystal physics coordinate system, using the thermodynamic theory of the electro-optic effect [31], r_{131} can be expressed as:

$$r_{131} = \left(\frac{\partial B_{13}}{\partial E_1}\right) \tag{1}$$

The electro-optic response originates from the coupling between the lattice polarization and the optical dielectric stiffness, $B_{ij} \cong g_{ijkl} P_k^L P_l^L$, where P_i^L is the lattice polarization and g_{ijkl} is the quadratic polar-optic tensor. The in-plane polarization component, P_1^L will change the most when applying an electric field (E_1) along the [100] direction, which directly relates to rotations of the index ellipsoid. This is quantified by $B_{13} \cong 2g_{1313} P_3^L P_1^L$. Under low fields, P_1^L responds linearly with E_1: $P_1^L \cong P_1^{L,0} + \chi_{11}^L E_1$. This gives a low-field linear electro-optic coefficient, $r_{131}^{lf} = 2g_{1313}\ P_3 \chi_{11}^L$. The same is true of the high-field linear electro-optic coefficient beyond the switching field, where P_1^L similarly responds linearly with E_1. The lattice dielectric susceptibility χ_{11}^L is maximized near the tetragonal-to-monoclinic phase boundary [8, 32]. This enhancement leads to the peak in r_{lf} and r_{hf} electro-optic response at the phase transition temperature. Figure S17 shows the phase-field simulated temperature-strain phase diagram of $KNbO_3$ represented in terms of a heat map of r_{131}^{lf}. As expected, the phase boundary between the tetragonal and monoclinic phases shows the highest low-field electro-optic response.

In contrast, as the applied electric field approaches the coercive field, the linear approximation of P_1^L with respect to E_1 breaks down: the net polarization vector undergoes large rotations in the swaying regime, producing a step-like Δn vs. E_{AC} response and a large effective electro-optic coefficient r_{max} at the onset of the step. The magnitude of this step, and hence the switching-driven electro-optic coefficient, r_{max}, scales with $P_1^{L,0}$, the in-plane polarization component at no applied electric field. $P_1^{L,0}$ increases as the temperature is decreased and the polarization tilts further away from the [001] direction in the monoclinic phase. This is further elucidated by a phase-field simulated temperature-strain heatmap of r_{131}^{max} which shows maximum response in the monoclinic phase away from the tetragonal-monoclinic phase boundary in contrast to r_{131}^{lf}. (Figure S17).

16163028, 0, Downloaded from https://advanced.onlinelibrary.wiley.com/doi/10.1002/adfm.79070, Wiley Online Library on [16/11/2026]. See the Terms and Conditions (https://onlinelibrary.wiley.com/terms-and-conditions) on Wiley Online Library for rules of use; OA articles are governed by the applicable Creative Commons License

Figure 2d shows the experimentally measured temperature dependence of r_{max} compared to phase-field simulations, reaching 43 000 pm V^{-1} at 5 K. This represents a 1000× improvement over the linear electro-optic response of industry-standard $LiNbO_3$, a 100× improvement over bulk $KNbO_3$, and a 20× improvement over a similar switching-driven electro-optic response reported for monoclinic $BaTiO_3$ thin films, establishing the highest electro-optic coefficient reported in any material to date. Such a multi-regime electro-optic response is further reproduced in a second $KNbO_3$ on $GdScO_3$ sample with $r_{max} = 40\,416 \pm 3533$ pm V^{-1}(Figure S12).

It is important to note that while r_{lf} and r_{hf} maximize at the tetragonal-to-monoclinic phase transition temperature (~275 K), r_{max} increases monotonically as the temperature is lowered. The linear electro-optic coefficients r_{lf} and r_{hf} are driven by the lattice dielectric susceptibility χ_{11}^{L}, which peaks at the phase transition temperature. This is also observed in $BaTiO_3$ thin films, where the electro-optic coefficient maximizes near the tetragonal-to-orthorhombic transition temperature. In contrast, r_{max} scales with the change in in-plane polarization upon switching between degenerate monoclinic variants, which increases with $P_1^{L,0}$, the in-plane polarization component at no applied electric field. $P_1^{L,0}$ increases as the temperature is decreased in the monoclinic phase, leading to an increase in r_{max}. A comparison between the experimentally measured r_{max} and the phase-field simulated $P_1^{L,0}$ as a function of temperature is shown in Figure S15.

The observed nonlinear electro-optic response also gives rise to higher-harmonic electro-optic effects, beyond the first-harmonic response observed in Figure 2a. These higher-harmonic responses are observed at 5 K (monoclinic phase), while for the tetragonal phase at 300 K no higher-harmonic responses are observed, consistent with the linear electro-optic response at 300 K (Figure S16).

To practically access this large switching-driven electro-optic response, the system requires biasing with a DC electric field (E_{DC}) to the vicinity of the switching instability, upon which E_{AC} drives the polarization swaying and produces a large Δn modulation. While r_{max} represents the maximum achievable switching-driven electro-optic response calculated from the maximum slope of the Δn vs. E_{AC} curve corresponding to an infinitesimal E_{AC} applied at the switching point (Figure 2b), in practice, a finite AC amplitude window will see a smaller slope. This reduces the observed switching-driven electro-optic coefficient, r_{mod}, while preserving the large Δn change. Figure 2d shows the temperature dependence of r_{mod} calculated using $E_{AC} = 1.25$ kV cm^{-1} centered around the switching field, reaching ~23 000 pm V^{-1} at 5 K.

4 | Hysteresis of the Electro-Optic Response

Next, we discuss the hysteresis and stability of this switching-driven electro-optic response. Figure 3a shows the experimentally measured electro-optic response while sweeping E_{DC} and keeping a fixed $E_{AC} = 1.25$ kV cm^{-1}. In the monoclinic phase, the electro-optic response is hysteretic, consistent with an in-plane polarization switching-driven swaying mechanism. The peak r_{mod} reaches 21 500 pm V^{-1} at 5 K, consistent with r_{mod} calculated from the Δn vs. E_{AC} measurements. Additionally, E_{DC} at which r_{mod} maximizes coincides with the inflection field of the Δn vs. E_{AC} curves (Figure S17). Closer to the monoclinic-to-tetragonal transition temperature (200 K), the hysteresis loop narrows, reflecting a more continuous switching pathway consistent with the temperature variation of the Δn vs. E_{AC} curves (Figure S8). Above the transition temperature, in the tetragonal phase (300 K), E_{DC} has no measurable effect on the electro-optic response, as expected in the absence of polarization swaying and a linear Δn vs. E_{AC} curve (Figure 2a). Phase-field simulations of the hysteresis of the r_{51} electro-optic coefficient (Figure 3b) reproduce this behavior across all three temperature regimes, capturing both the hysteretic switching response in the monoclinic phase and its suppression in the tetragonal phase.

To relate the observed hysteretic response to the underlying domain evolution, phase-field simulations of the domain microstructure under applied electric fields were performed (Figure 3c). The starting microstructure is poled along [$\bar{1}$00] at $E_{DC}/E_C = 0$. In this scenario, the P_1 polarization component of all unit cells lies along the [$\bar{1}$00] direction with an equal number of unit-cells having P_2 polarization component along [010] and [0$\bar{1}$0] directions, giving an average $P_2 \cong 0$. Under an applied electric field E_1 along the [100] direction, this microstructure evolves through the switching field ($E_{DC}/E_C = 1.7$) into a configuration where the unit cells with initial P_1 polarization along [$\bar{1}$00] variants switch to $P_1 \| [100]$. Eventually at $E_{DC}/E_c = 3.2$, the average P_1 polarization component has switched from [$\bar{1}$00] to [100] while the P_2 component is unchanged in comparison to the starting microstructure. This is further illustrated in Video S2.

This polarization switching is accompanied by a reversal of the $\epsilon_{13}^{optical}$ component of the optical dielectric tensor that mimics the polarization microstructure (Figure 3c). This is further demonstrated in Video S3. The resultant reorientation of the index ellipsoid because of the switching process, calculated from the microstructure-averaged optical dielectric tensor, is illustrated in Video S1. The sign change of $\epsilon_{13}^{optical}$ concurrent with the polarization switching reflects the reorientation of the optical index ellipsoid between the two domain configurations and corresponds to a sign change in $B_{13} = (\frac{1}{\epsilon^{optical}})_{13}$. The rate of change dB_{13}/dE_1 is maximized at the switching field, giving rise to the peak in r_{51} observed in Figure 3a,b. At temperatures closer to the transition, the switching becomes more continuous, with the sign change in $\epsilon_{13}^{optical}$ occurring more smoothly with field. This accounts for the reduced r_{max} electro-optic response observed at higher temperatures. The polarization microstructure evolution is further visualized in the phase-field simulated stereographic projections (Figure 3d). The color intensity represents the number of unit cells with polarization pointed along a certain direction when averaged across the entire microstructure. This temporal evolution of the stereographic projection under switching is further demonstrated in Video S4.

5 | Stability of the Electro-Optic Response

Optical switching applications require electro-optic modulations at frequencies of MHz or more. Figure 4a shows the Δn vs. E_{AC} curves measured at 5 K across a range of frequencies from 555 Hz to 1 MHz. The switching response and Δn magnitude change

16163028, 0, Downloaded from https://advanced.onlinelibrary.wiley.com/doi/10.1002/adfm.79070, Wiley Online Library on [16/11/2026]. See the Terms and Conditions (https://onlinelibrary.wiley.com/terms-and-conditions) on Wiley Online Library for rules of use; OA articles are governed by the applicable Creative Commons License

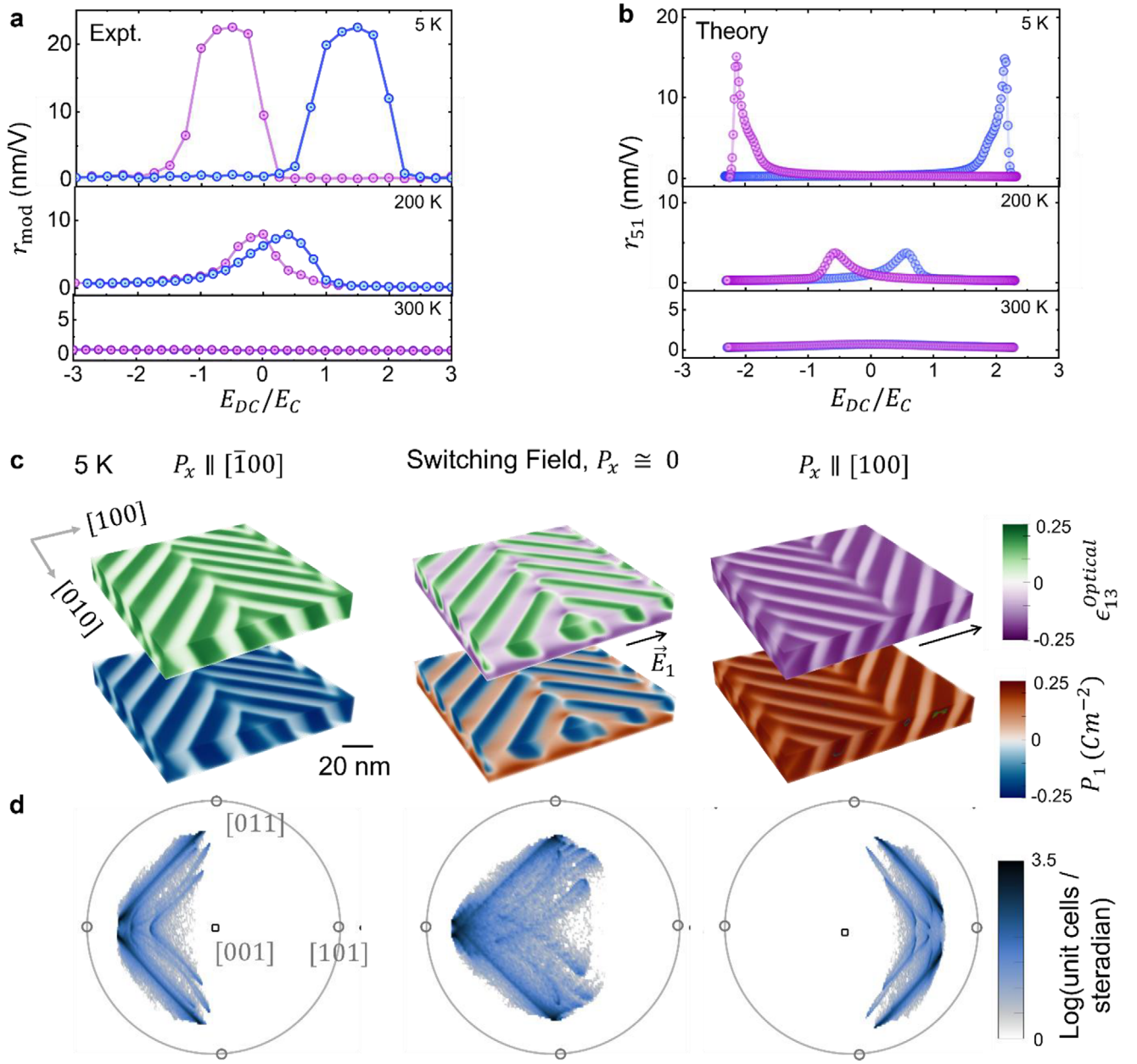


FIGURE 3 | (a) Experimentally measured r_{mod} as a function of E_{DC}/E_C at three temperatures 5 K, 200 K, and 300 K measured with a fixed AC modulation amplitude of 1.25 kV cm^{-1}. In the monoclinic phase, the response is hysteretic, consistent with a switching-driven mechanism, with a peak r_{mod} of 23 000 pm V^{-1} at 5 K. The hysteresis loop narrows closer to the transition temperature (200 K), and eventually no hysteresis is observed in the tetragonal phase (300 K). (b) Phase-field simulated r_{51} vs. E_{DC}/E_C at the same three temperatures, consistent with the experimentally observed behavior across all three temperatures. (c) Phase-field simulated microstructure of optical dielectric tensor component $\epsilon_{13}^{optical}$ (top) and in-plane polarization P_1(bottom) at 5 K for three electric field values: P_1 poled along [$\bar{1}$00] ($E_{DC}/E_C = 0$), at the switching field ($E_{DC}/E_C = 1.7$), and P_1 poled along [100] ($E_{DC}/E_C = 3.2$). The sign changes of $\epsilon_{13}^{optical}$ at the switching field drives the peak in r_{51}. This is further illustrated in Videos S2 and S3. (d) Phase-field simulated stereographic projections at the same three field values, representing the number of unit cells with polarization per unit solid angle (steradians), projected onto the (001) plane. The complete field-dependent stereographic projection is shown in Video S4.

across the switch is preserved throughout the entire measured frequency range, with the coercive field increasing from ~ 2.5 to ~ 3.5 kV cm^{-1} as the modulation frequency is increased. The corresponding frequency dependence of r_{max} and r_{lf} remain stable across the full frequency range measured (Figure 4b). Additionally, Figure S18 shows the modulation frequency dependence of the electro-optic response at 300 K, demonstrating a stable electro-optic response.

The 1 MHz upper limit demonstrated here reflects the bandwidth of our current free-space measurement setup rather than an intrinsic material constraint. The enhanced MHz frequency electro-optics performance is already useful for photonic switching and signal routing applications. For achieving exceptional electro-optic performance driven by the polarization swaying mechanism in the GHz regime, the ionic motions contributing to the swaying must respond at the desired frequency. Prior

16163028, 0, Downloaded from https://advanced.onlinelibrary.wiley.com/doi/10.1002/adfm.79070, Wiley Online Library on [16/11/2026]. See the Terms and Conditions (https://onlinelibrary.wiley.com/terms-and-conditions) on Wiley Online Library for rules of use; OA articles are governed by the applicable Creative Commons License

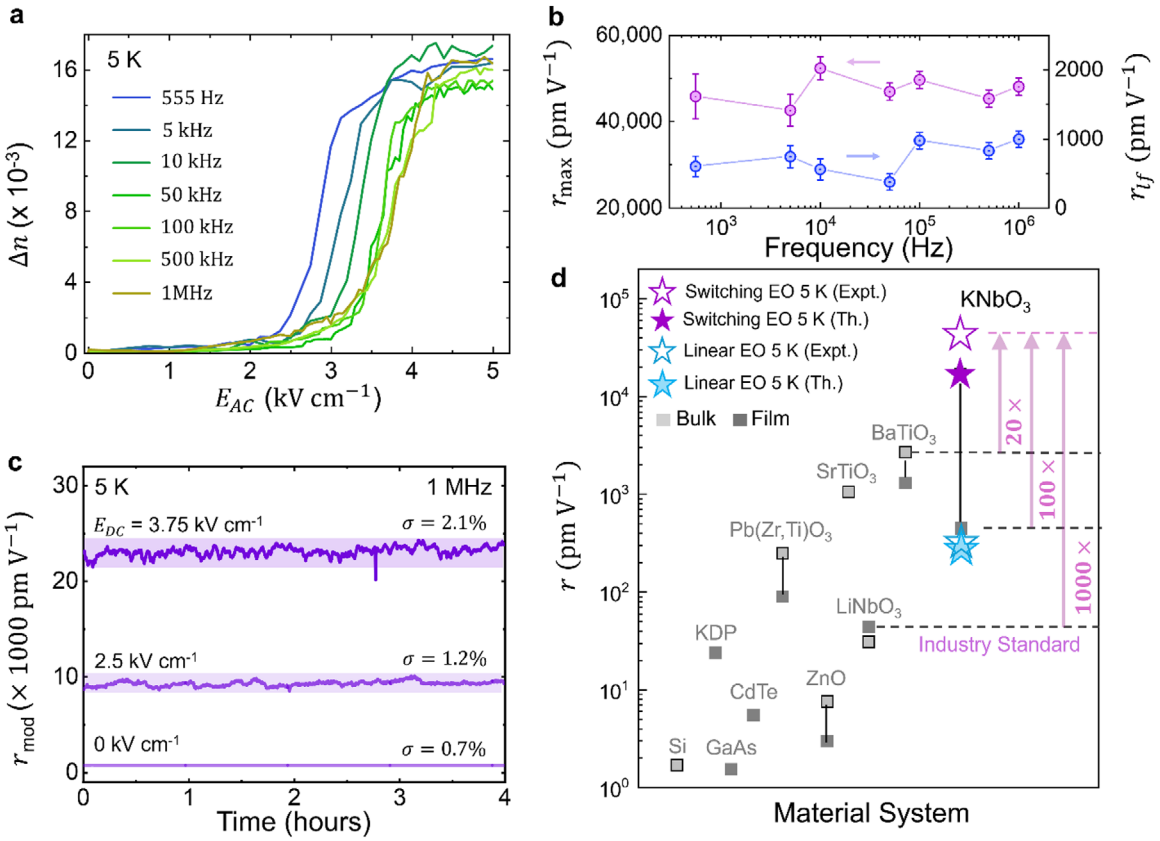


FIGURE 4 | (a) Experimentally measured Δn vs. E_{AC} at 5 K across frequencies from 555 Hz to 1 MHz. The switching response and Δn magnitude is preserved across the entire frequency range, while the coercive field increases. (b) Frequency dependence of r_{max} and r_{lf} from 555 Hz to 1 MHz at 5 K. (c) Temporal stability of r_{mod} measured at 5 K at three fixed E_{DC} bias points (0, 2.5, and 3.75 kV cm^{-1}) over 4 h, yielding standard deviations of 0.7%, 1.2%, and 2.1%, respectively. (d) Comparison of the linear and switching-driven electro-optic coefficient of $KNbO_3$/$GdScO_3$ (experimental and phase-field, 5 K) against the landscape of bulk and thin-film electro-optic materials [8, 45–50, 26, 12, 51], establishing the highest electro-optic coefficient reported in any material to date, 1000× higher than the linear electro-optic coefficient of industry-standard $LiNbO_3$.

work in related materials has demonstrated that ferroelectric dynamics such as polarization rotation [33–35], domain wall displacements between low-symmetry phases [34], and polarization switching [36–38] in related materials can extend up to GHz and subterahertz frequencies. This implies that GHz frequency operational bandwidth is achievable for such exceptional electro-optic responses driven by polarization swaying.

A low coercive field of $\sim$ 1 kV cm^{-1} could lead to instabilities in the observed switching-driven electro-optic response due to bias drifts or domain reconfiguration. To test this, the temporal stability of the switching-driven electro-optic response was characterized by measuring r_{mod} with different applied E_{DC} bias points with a fixed E_{AC} of 1.25 kV cm^{-1} at 1 MHz over 4 h (Figure 4c). The different bias points represent different operational regimes across the Δn vs. E_{AC} curves. These measurements yield standard deviations of 0.7%, 1.2%, and 2.1% of their respective r_{mod} corresponding to an E_{DC} of 0, 2.5, and 3.75 kV cm^{-1} respectively. To assess the reproducibility of the electro-optic response, r_{max}, r_{lf} and r_{mod} were measured under both electrical and thermal cycling. For electrical cycling tests, the sample was fatigued through multiple electrical cycles between every measurement, as shown in Figure S19 and Tables S4,S5. All three coefficients exhibit stable responses under electrical field cycling up to 10^8 cycles. For thermal cycling, Δn vs. E_{AC} curves were measured at 5 K, followed by heating up to room temperature and subsequently cooling down before remeasuring. Under thermal cycling, larger cycle-to-cycle variations are observed, suggesting that each thermal cycle resets the domain configuration. Once the ground state domain microstructure is established upon cooling, both the linear and switching-driven electro-optic response remains robust under subsequent electrical field cycling. Additionally, stability of the hysteretic electro-optic response was confirmed under E_{DC} cycling as shown in Figure S19.

6 | Discussion

For photonic device integrations, the r_{11} electro-optic coefficient with an in-plane change in refractive index, Δn_{11}, is more favorable. This can be extracted from normal incidence electro-optic measurements (see Supporting Information). For the tetragonal phase with an out-of-plane polarization, r_{11} is forbidden (see Supporting Information). In comparison, r_{11} can exist in the low-temperature monoclinic phase. Δn vs. E_{AC} curves are measured in normal incidence show a multi-regime response at 5 K, as shown in Figure 5a, yielding r_{max} = 2670 pm V^{-1} extracted from the step-like switching regime. In normal incidence, the observed electro-optic response is dominated by the r_{11} electro-optic response (see Supporting Information). The linear optical

16163028, 0, Downloaded from https://advanced.onlinelibrary.wiley.com/doi/10.1002/adfm.79070, Wiley Online Library on [16/11/2026]. See the Terms and Conditions (https://onlinelibrary.wiley.com/terms-and-conditions) on Wiley Online Library for rules of use; OA articles are governed by the applicable Creative Commons License

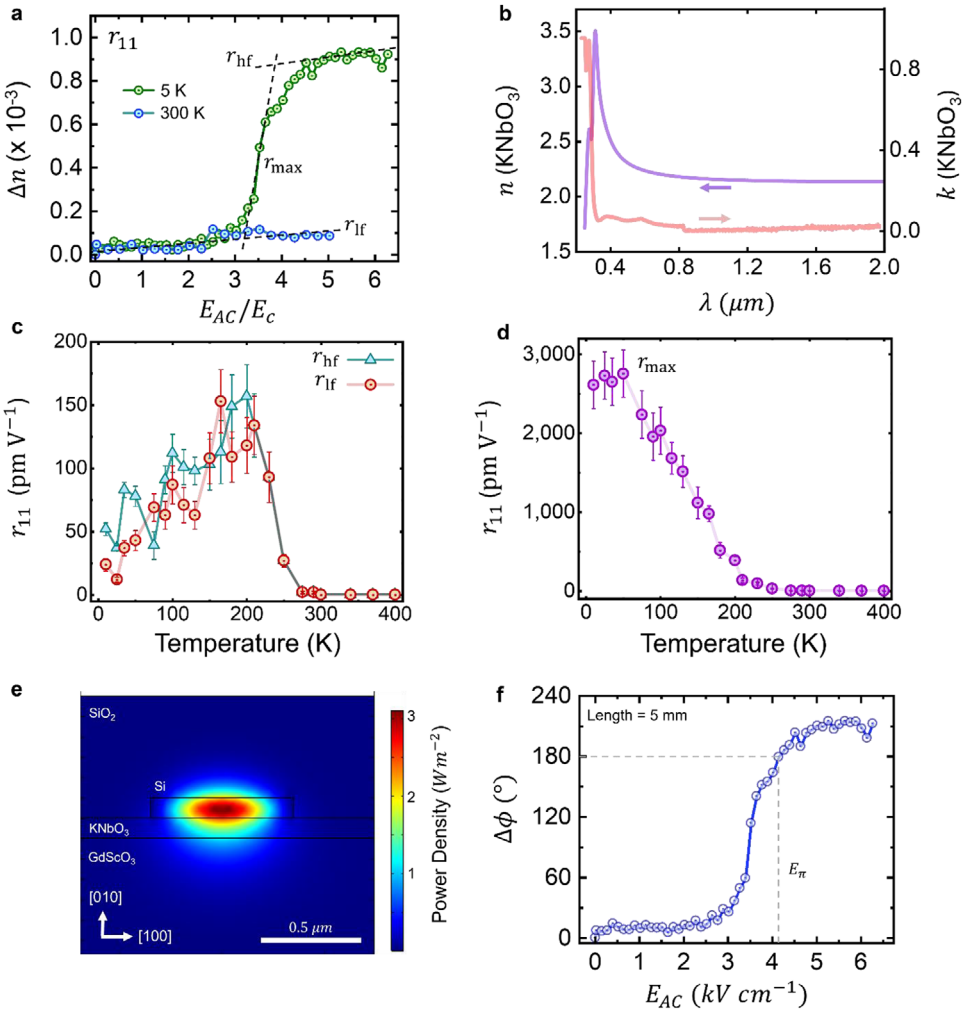


FIGURE 5 | (a) Δn vs. E_{AC}/E_C measured at normal incidence at 5 and 300 K, where $E_C = 1\ kV\ cm^{-1}$. No electro-optic response is observed at 300 K, while a multi-regime response is observed at 5 K with $r_{max} \sim 2670\ pm\ V^{-1}$, $r_{lf} \sim 26\ pm\ V^{-1}$ and $r_{hf} \sim 63\ pm\ V^{-1}$. The observed Δn at 5 K can be attributed to the r_{11} electro-optic coefficient (see Supporting Information). (b) Refractive index, n, and extinction coefficient, k, for the $KNbO_3$ film at 300 K. n is measured using spectroscopic ellipsometry, while k is measured using UV–vis transmission (Figure S11). (c) Temperature dependence of r_{lf} and r_{hf}. (d) Temperature dependence of r_{max}. (e) COMSOL-simulated cross-sectional Power density of the TE_{00} mode through a 100 nm silicon ridge waveguide on a 100 nm thick $KNbO_3$ film on $GdScO_3$. The parameters used for simulations are shown in Table S7. (f) COMSOL simulated phase change ($\Delta\phi$) of light across a waveguide with $L = 5\ mm$, with $E_\pi = 4.1\ kV\ cm^{-1}$.

response of the $KNbO_3$ film measured by spectroscopic ellipsometry and UV–vis is shown in Figure 5b (see Supporting Information). Figure 5c shows the temperature dependence of the extracted r_{lf} and r_{hf} coefficients measured in normal incidence electro-optic measurements (Figure 5a). Similar to oblique incidence measurements (Figure 2c), r_{lf} and r_{hf} maximize at the tetragonal-monoclinic phase boundary. In contrast, Figure 5d shows the temperature dependence of r_{max} which emerges below the tetragonal-to-monoclinic phase transition temperature and grows as the temperature is lowered.

To estimate the phase-modulation performance, COMSOL simulations of a silicon ridge waveguide hosting a transverse electric (TE_{00}) mode were performed, as shown in Figure 5e. Similar to conventional waveguides on electro-optic $BaTiO_3$ thin films, a 100 nm thick silicon waveguide is modeled on a 100 nm thick $KNbO_3$ thin film on $GdScO_3$ (see Supporting Information). From the experimentally measured Δn in normal incidence electro-optic measurements (Figure 5a), the simulated phase change (ϕ) of light across a waveguide length of $L = 0.5\ cm$ is shown in Figure 5f. The electric field, E_π, required for a phase change, $\Delta\phi = \pi$, is $\sim$ 4.1 kV cm^{-1}. For a 0.7 μm thick waveguide this gives a half-wave voltage, $V_\pi = 0.28\ V$ and hence $V_\pi.L = 0.14\ Vcm$. The simulated $V_\pi.L = 0.14\ Vcm$ for monoclinic $KNbO_3$ represents a 36× improvement over cryogenic EO modulator based on $BaTiO_3$ thin films on silicon with $V_\pi.L = 5\ Vcm$ at 4 K [7], and a 16× improvement over room-temperature $LiNbO_3$ modulators with $V_\pi.L = 2.2\ Vcm$ [39].

To access the large switching-driven electro-optic enhancements at room temperature, enabled by the polarization swaying mechanism, it is necessary to establish the monoclinic phase at room temperature. When $KNbO_3$ is grown on $GdScO_3$ (biaxial compressive strain, $\varepsilon \sim -1.1\%$), the tetragonal-to-monoclinic phase transition is observed at $\sim$ 275 K. From the phase-field simulated phase diagram (Figure S20), when $KNbO_3$ is grown

16163028, 0, Downloaded from https://advanced.onlinelibrary.wiley.com/doi/10.1002/adfm.79070, Wiley Online Library on [16/11/2026]. See the Terms and Conditions (https://onlinelibrary.wiley.com/terms-and-conditions) on Wiley Online Library for rules of use; OA articles are governed by the applicable Creative Commons License

under lower compressive strains ($|\varepsilon| < 0.8\%$), the tetragonal-to-monoclinic phase transition temperature can be increased above room temperature.

These strain states can be accessed by growing $KNbO_3$ on compositionally graded (Ba,Sr)TiO_3-buffered silicon substrates. Bulk $SrTiO_3$ has a lattice parameter of 3.905 Å, while $BaTiO_3$ has a lattice parameter of 4.005 Å. For Ba concentrations exceeding $x = 0.7$ in compositionally graded $(Ba_xSr_{1-x})TiO_3$ buffer layers, the imposed compressive strain on $KNbO_3$ falls below 0.8%, sufficient to stabilize the monoclinic phase above room temperature according to the phase diagram (Figure S20). Alternatively, compositionally graded $SrSn_xTi_{1-x}O_3$ or $SrGe_xTi_{1-x}O_3$ buffer layers can also be used to achieve a similar lattice parameter tuning [40, 41].

7 | Conclusion

In summary, compressive epitaxial strain in $KNbO_3$ thin films stabilizes a monoclinic phase that enables an electro-optic mechanism driven by polarization swaying superior to the conventional Pockels response relying on a linear coupling between electric field and polarization. The associated reorientation of the optical index ellipsoid between degenerate monoclinic variants yields an electro-optic coefficient of $\sim 43\,000$ pm V^{-1} at 5 K, establishing the highest electro-optic coefficient reported in any material to date. Figure 4d shows the linear (r_{lf}, r_{hf}) and the switching-driven (r_{max}) electro-optic response measured in $KNbO_3$ in comparison to the linear electro-optic response of standard materials, demonstrating the electro-optic enhancement enabled by such a polarization swaying-driven mechanism. The ultralow polarization switching barriers of $\sim$ 1 kV cm^{-1} are well within the range of standard driving fields of electronic devices. The operation is demonstrated up to 1 MHz, along with its temporal stability over hours and robustness under electrical and thermal cycling. Importantly, this approach can be extended to silicon-compatible platforms either through straining $KNbO_3$ films on compositionally graded (Ba,Sr)TiO_3-buffered silicon substrates [42, 43] or through (K,Na)NbO_3 solid solutions [44] that can host monoclinic phases even without requiring strain tuning. Additionally, the monoclinic phase transition temperature can be modified by strain or compositional tuning depending on the desired operating temperature. This is promising for MHz photonic switching, optical signal routing, and cryogenic optical interconnects for quantum computing systems. The large polarization susceptibility inherent to low-symmetry ferroelectric phases unlock a largely unexplored materials design space for energy-efficient, high-speed photonic integrated circuits operating from room to cryogenic temperatures.

8 | Methods

8.1 | Thin Film Synthesis

Epitaxial thin films of $KNbO_3$ were grown using a Vecco Gen 10 MBE system. A molecular beam of NbO_2 (gas) flux was generated from an effusion cell containing Nb_2O_5 (H.C. Stark 99.99%) contained in an iridium crucible. NbO_2 is the most volatile species in the growth temperature range [52]. Potassium was evaporated from an effusion cell containing an indium-rich (about 4:1 In:K ratio) mixture of potassium and indium so that it forms the air-stable intermetallic In_4K [53]. The K-In alloy was prepared in a glove box and contained in a titanium crucible. Once prepared, it can be exposed to air, facilitating its handling and loading. The vapor pressure of potassium is more than 10^{10} times higher than indium at the K-In cell temperature of 300°C–400°C [54]. $GdScO_3$ $(110)_o$ (Crystec GmbH) substrates were used as received.

Films were grown by co-deposition of potassium, NbO_2, and ozone at a substrate temperature of 650°C to 700°C as measured by an optical pyrometer operating at a wavelength of 1550 nm. The pyrometer measures the temperature of the platinum coating that has been evaporated on the backside of the substrate to facilitate radiative heat transfer from the SiC heating element of the MBE system to the substrate. The K/Nb flux ratio was kept at approximately 10:1. A mixture of ozone and oxygen (10% O_3 + 90% O_2) was used as an oxidant. The films were grown at an oxidant background pressure of 1×10^{-6} Torr. Typical fluxes for the sources were $(1-2)\times 10^{13}$ atoms cm^{-2} s^{-1} for NbO_2 and $(1-4)\times 10^{14}$ atoms cm^{-2} s^{-1} for potassium, determined by a quartz crystal microbalance (QCM), with an accuracy of about 15%. In a typical growth experiment, the potassium flux was measured first, followed by NbO_2 to ensure that the QCM was as close to room temperature as possible for the most accurate reading. For a more detailed description, the reader is referred to an identical procedure reported for $KTaO_3$ [55]. Co-deposition with these fluxes results in a $KNbO_3$ film growth rate of about 0.3 Å s^{-1}.

X-ray diffraction (XRD), X-ray reflectometry (XRR), and RSM measurements were carried out using a PANalytical Empyrean diffractometer with Cu $K\alpha_1$ radiation. The raw XRR spectra were analyzed using the PANalytical X´Pert Reflectivity software package, and the layer thickness was derived from a fast Fourier transform (FFT) after manually defining the critical angle to account for refractive effects. In situ reflection high-energy electron diffraction (RHEED) patterns were recorded using KSA-400 software and a Staib electron source operated at 14 kV and a filament current of 1.5 A. Figure S1 shows RHEED patterns, XRD patterns, and transmission electron microscopy of the $KNbO_3$ film grown on $GdScO_3$. Further details of thin film synthesis and characterization are discussed elsewhere [14].

8.2 | Phase-Field Simulations

Based on the thermodynamic theory of optical properties, we may formulate a phase-field model, where the thermodynamics of the ferroelectric system is described by its free energy functional,

$$F = \int \left[f^L\left(T,\, P_i^L\right) + f^e\left(T,\, P_i^e\right) + f^{L-e}\left(P_i^L,\, P_i^e\right) + f^{grad}\left(\nabla_i P_j^L\right) + f^{elas}\left(P_i^L,\, P_i^e,\, \varepsilon_{ij}\right) + f^{elec}\left(P_i^L,\, P_i^e,\, E_i\right)\right] dx^3 \quad (2)$$

where $P_i^L(x_i,\, t)$ is the lattice polarization, $P_i^e(x_i,\, t)$ is the electrical polarization, and $\sigma_{ij}(x,t)$ is the stress [31]. The respective evolution of the lattice polarization and electronic polarization is solved separately.

16163028, 0, Downloaded from https://advanced.onlinelibrary.wiley.com/doi/10.1002/adfm.79070, Wiley Online Library on [16/11/2026]. See the Terms and Conditions (https://onlinelibrary.wiley.com/terms-and-conditions) on Wiley Online Library for rules of use; OA articles are governed by the applicable Creative Commons License

The lattice polarization is computed following the relaxational approximation, where we assume relaxational kinetics for the lattice polarization, and the mechanical displacement, electrical potential, and electrical polarization instantaneously reach equilibrium, leading to the time-dependent Ginzburg–Landau equation

$$\gamma_{ij}^{L}\frac{\partial P_j^L}{\partial t} = -\frac{\delta F}{\delta P_i^L}, \tag{3}$$

where $-\frac{\delta F}{\delta P_i^L}$ is the thermodynamic driving force for the temporal evolution of the lattice polarization. We use the local stress and lattice polarization distribution as inputs to the electronic polarization dynamic equation

$$\mu_{ij}^{e}\frac{\partial^2 P_j^e}{\partial t^2} + \gamma_{ij}^{e}\frac{\partial P_j^e}{\partial t} = -\frac{\delta F}{\delta P_i^e}, \tag{4}$$

where $-\frac{\delta F}{\delta P_i^e}$ is the thermodynamic driving force for the temporal evolution of the electronic polarization. To compute the local electronic dielectric susceptibility, we solve Equation (4) assuming a small periodic electric field is applied, which yields an analytical solution

$$\widetilde{\chi_{ij}^{e,1}}\left(x_i,\,\omega\right) = \left[B_{ij}^{e}\left(x_i\right) - \epsilon_0\left(i\omega\gamma_{ij}^{e} + \omega^2\mu_{ij}^{e}\right)\right]^{-1} \tag{5}$$

which is related to the curvature of the free-energy landscape with respect to the electronic polarization by, $B_{ij}^{e}\left(x_i\right) = \epsilon_0\left(\frac{\partial^2 f}{\partial P_i^e,\,\partial P_j^e}\right)$, where f, is the free energy density. Solving Equation (5) (assuming $\lambda = 1550\ nm$) we may compute the local refractive indices from the local lattice polarization and stress distribution, thereby naturally including the electro-optic effect and potential piezo-optic effects. As the lattice polarization distribution evolves in response to an applied electric field, the corresponding change to the electronic dielectric susceptibility and the refractive index is computed.

Here $f^L(P_i^L)$ describes the intrinsic stability of the lattice polarization compared to the high-symmetry phase ($m\bar{3}m$) as a Taylor expansion of the polarization about the high-symmetry phase, this is equivalent to the Landau free energy density:

$$\begin{aligned} f^{L}\left(T,\,P_i^L\right) = {} & f_o + a_{ij}\left(T\right)P_i^L P_j^L + a_{ijkl}P_i^L P_j^L P_k^L P_l^L \\ & + a_{ijklmn}P_i^L P_j^L P_k^L P_l^L P_m^L P_n^L \\ & + a_{ijklmnop}P_i^L P_j^L P_k^L P_l^L P_m^L P_n^L P_o^L P_p^L \end{aligned} \tag{6}$$

where a_{ij}, a_{ijkl}, a_{ijklmn} and $a_{ijklmnop}$ are the dielectric stiffness coefficients measured under constant stress conditions. For $KNbO_3$, an eighth-order expansion is used to describe the stability of the lattice polarization [32].

The intrinsic free energy density of the electronic polarization, in the absence of the lattice polarization, is described by

$$f^{e}\left(T,\,P_i^e\right) = \frac{1}{2\epsilon_0}B_{ij}^{e,ref}\left(T\right)P_i^e P_j^e \tag{7}$$

where $B_{ij}^{ref}(T)$ is related to the refractive index of the equivalent high-symmetry phase. The coupling energy density between the lattice and electronic polarization, which determines the electro-optic effect, is given by

$$f^{L-e}\left(P_i^L,\,P_i^e\right) = \frac{1}{2\epsilon_0}g_{ijkl}^{LL}P_l^L P_k^L P_i^e P_j^e \tag{8}$$

where g_{ijkl}^{LL} relates the lattice polarization to the refractive index.

The gradient energy density is represented by

$$f_{grad} = \frac{1}{2}G_{ijkl}\frac{\partial P_i^L}{\partial x_j}\frac{\partial P_k^L}{\partial x_l} \tag{9}$$

where G_{ijkl} is the gradient energy tensor where the non-zero coefficients are chosen to be $G_{11} = 0.6$, $G_{22} = -0.6$ and $G_{44} = 0.6$, and the units are normalized by $\alpha_1 l_o^2$, where α_1 is the first Landau expansion coefficient and l_o is chosen as 1 nm per grid point.

The elastic energy is given by

$$f^{elas}\left(P_i^L,\,P_i^e,\,\sigma_{ij}\right) = \frac{1}{2}C_{ijkl}\left(\varepsilon_{ij} - \varepsilon_{ij}^{o}\right)\left(\varepsilon_{kl} - \varepsilon_{kl}^{o}\right) \tag{10}$$

where C_{ijkl} is the elastic stiffness, ε_{ij} is the total strain, and $\varepsilon_{ij}^{o} = Q_{ijkl}\sigma_{ij}P_k^L P_l^L + \frac{1}{2\epsilon_0}\pi_{ijkl}\sigma_{ij}P_k^e P_l^e$ is the eigenstrain, where Q_{ijkl} is the electrostrictive coefficient and π_{ijkl} is the piezo-optic tensor for the high-symmetry phase. The total strain is solved for a thin film boundary condition assuming that the strain relaxes to its equilibrium value at each time step; for simplicity, we ignore the contribution of the electronic polarization to the eigenstrain. Further details on solving the elasticity may be found in reference [56].

The electrostatic energy is given by

$$f^{elec} = -E_i P_i^L - E_i P_i^e - \frac{1}{2}\epsilon_0\kappa_{ij}^{b}E_i E_j \tag{11}$$

where ϵ_0 is the vacuum permittivity and κ_{ij}^{b} is the background dielectric constant. For simplicity, to compute the evolution of the lattice polarization, we only include the linear contribution to electronic polarization and add it to the background dielectric constant, yielding $f^{elec} = -E_i P_i^L - \frac{1}{2}\epsilon_0\kappa_{ij}^{b}E_i E_j$, where $\kappa_{ij}^{b} = 10$ and is isotropic. Here κ_{ij}^{b} contains contributions from the electronic contribution and the vacuum and other hard modes. A table containing all coefficients used in the phase-field simulations is given in the Table S6).

For the simulations, a system size of 128 Δx_1 128 Δx_2 × 36 Δx_3 is used. There are 12 Δx_3 grid points for the substrate where the elastic constants are assumed to be the same as the ferroelectric film, and there are 4 Δx_3 grid points acting as an air layer above the film. The thickness of $KNbO_3$ is set to be 20 Δx_3. Periodic boundary conditions are used along the in-plane lateral directions, and natural boundary conditions are used along the film-substrate and film-air interfaces. The interface between the film and the substrate is assumed to be coherent, and hence the misfit strain is calculated using the equivalent cubic lattice parameters for $KNbO_3$ and the pseudocubic lattice parameters for

16163028, 0, Downloaded from https://advanced.onlinelibrary.wiley.com/doi/10.1002/adfm.79070, Wiley Online Library on [16/11/2026]. See the Terms and Conditions (https://onlinelibrary.wiley.com/terms-and-conditions) on Wiley Online Library for rules of use; OA articles are governed by the applicable Creative Commons License

$GdScO_3$ [14].

$$\varepsilon_{11} = \frac{a^{[110]_o}_{GdScO3} - a^{eq}_{KNbO3}}{a^{eq}_{KNbO3}}, \quad \varepsilon_{22} = \frac{a^{[001]_o}_{GdScO3} - a^{eq}_{KNbO3}}{a^{eq}_{KNbO3}} \quad \varepsilon_{12} = \varepsilon_{21} = 0 \tag{12}$$

where the lattice parameters for $KNbO_3$ are $a^{eq}_{KNbO3}(T) = 4.004\,\forall + 2.657 \times 10^{-5} \forall\, T$ and $GdScO_3$ are $a^{[110]_O}_{GdScO3}(T) = 3.970\,\forall\,(1 + 1.09 \times 10^{-5}(T - 300\text{ K}))$ and $a^{[001]_o}_{GdScO3}(T) = 3.966\,\forall\,(1 + 1.09 \times 10^{-5}(T - 300\text{ K}))$.

The simulations begin with an initial condition of $P^L_i(x_i,\ t = 0) = [0.0\ 0.0\ 0.1\ \text{C m}^{-2}] + \Delta P^{noise}(x_i,\ t = 0)$, where $|P^{noise}| = 0.1\ \text{C m}^{-2}$, and relax for 20 000 time steps. To simulate the evolution of the polarization under an applied electric field and the corresponding electro-optic effect, a uniform electric field is applied along the $[100]_{pc}$ direction, ranging from -70 to 70 kV cm^{-1} which varies in time with a sinewave, with one period of the being equal to 65 000 time steps. To simulate the field-dependent electro-optic coefficient at 5 K, a higher maximum electric field for 100 kV cm^{-1} is used to obtain the full range of electro-optic behavior. The linear electro-optic effect is found by taking the average of the refractive index over the ferroelectric material as a function of an applied electric field and fitting to a cubic polynomial centred at zero. The phase fractions were determined by sorting the local lattice polarization vectors according to the minimum angular deviation from the ideal crystallographic polarization directions, assuming the presence of only tetragonal, orthorhombic and rhombohedral domains. The lattice polarization evolution was computed using the Mu-Pro phase-field simulation package.

8.3 | Second Harmonic Generation

Temperature- and electric field-dependent SHG measurements were performed with a femtosecond pulsed laser at $\lambda = 800$ nm fundamental light from a regeneratively amplified Spectra-Physics Solstice Ace Ti:Sapphire laser system (1 kHz, 100 fs). The schematic of the setup is shown in Figure S2. Linearly polarized light incident on the sample at an incidence angle Θ generates second harmonic light at $\lambda = 400$ nm. The *p*-polarized and s-polarized SHG intensities are spectrally filtered and measured by a photomultiplier tube through lock-in amplifier (SR830) detection. Polar plots are generated by rotating the polarization angle (ϕ) of the incident fundamental light by a half-wave plate. Temperature-dependent measurements were done through a Janis 300 gas flow cryostat for low-temperature and a home-built heating stage for high-temperature experiments. For electric field-dependent measurements, electrodes with 60 μm gaps were used, and voltage was applied using an Agilent 33220A function generator (5 mHz triangular waves) amplified by a TREK 610C high-voltage amplifier.

8.4 | Synchrotron-Based Reciprocal Space Mapping

Synchrotron x-ray diffraction experiments were performed at the ID4B (QM2) beamline at the Cornell high-energy synchrotron source (CHESS). The incident X-ray energy was 20 keV, which was selected using a double-bounce diamond monochromator. An area detector array (Pilatus 6 M) was used to collect the scattering intensities in a reflection geometry. The sample was rotated with 1° tilt through 360° rotations, sliced into 0.1° frames. Geometric parameters of the Pilatus 6 M detector, such as detector distance, tilting, rotation, and direct beam position, were extracted using standard CeO_2 powder. The uncertainty in temperature is < 10 K.

8.5 | Temperature-Dependent Ellipsometry Measurements

Spectroscopic ellipsometry measurements were performed using a J. A. Woollam M-2000XI rotating-compensator, variable angle spectroscopic ellipsometer, with Ψ, Δ, and Mueller matrix parameters collected at incident angles of 45°, 55°, 65°, and 75°. Data were collected across a spectral range of 271.1 to 1689.3 nm, and analysis was performed with the J.A. Woollam CompleteEASE software (see Supporting Information). An Oxford MicrostatHe gas flow cryostat with a home-built vacuum shroud was used for temperature-dependent measurements.

8.6 | Electrode Deposition

$500 \times 500\ \mu m^2$ square electrode patterns with 200 μm spacings were prepared using a standard photolithography approach. LOR5a and SPR2012 photoresist were used with patterns written by Heidelberg MLA150 and were developed by CD26 developer solution. A 5 nm Ti adhesion layer and 150 nm Pt layer were deposited as electrodes using e-beam evaporation (Temescal FC-2000).

8.7 | Polarization-Based Electro-Optic Measurement

Electro-optic measurements were performed using a homebuilt polarizer-sample-compensator-analyzer setup with a 1550 nm HP 81689A continuous-wave laser source with an APD430C detector. For measurements below 100 kHz modulation frequency, a Stanford Research SR830 lock-in amplifier was used. For modulation frequencies above 100 kHz, a Stanford Research SR844 was used. A schematic of the setup used for our experiments is shown in Figure S5a. For absolute intensity measurements, a mechanical chopper was placed in the laser path and modulated at 1.54 kHz for detection with a Stanford SR830 lock-in amplifier. For measuring the modulated transmission intensity, an Agilent 33220A signal generator amplified by a Trek 610C high-voltage amplifier was used to apply a modulation signal at 555 Hz to the sample (~ 200 μm electrode gap size). Samples were cooled to liquid He temperatures using a Janis 30 continuous flow cryostat system. For modulation frequency-dependent measurements (555 Hz to 1 MHz), smaller electrode gap sizes (~ 10 μm) on the sample were used, and hence no voltage amplification was needed.

The polarization of the probe was set to lie between the ordinary and extraordinary refractive indices. An analyzer placed at the end of the setup was oriented orthogonal to the initial probe polarization state, resulting in no transmission of light through

16163028, 0, Downloaded from https://advanced.onlinelibrary.wiley.com/doi/10.1002/adfm.79070, Wiley Online Library on [16/11/2026]. See the Terms and Conditions (https://onlinelibrary.wiley.com/terms-and-conditions) on Wiley Online Library for rules of use; OA articles are governed by the applicable Creative Commons License

the setup when the sample and compensator were not included. With the sample introduced, the transmission becomes nonzero on account of the birefringence-induced ellipticity. A quarter-wave compensator was then added immediately after the sample to cancel out the native material birefringence with no voltage applied. This returns the transmission of the setup to zero until a voltage is applied to modulate the sample refractive indices and reintroduce ellipticity to the probe.

Author Contributions

Sankalpa Hazra: conceptualization, investigation, writing – original draft, writing – review and editing, visualization, validation, methodology, formal analysis, data curation. **Aiden Ross**: investigation, conceptualization, validation, methodology, writing – review and editing, visualization, software, formal analysis, data curation. **Ian Reed Philippi**: investigation, methodology, writing – review and editing. **Albert Suceava**: investigation, validation, writing – review and editing. **Himirkanti Sarkar**: investigation, validation, writing – review and editing. **Muhammed Aminul Haque Choudhury**: investigation, validation, writing – review and editing. **Long-Qing Chen**: writing – review and editing, funding acquisition, project administration, supervision, resources. **Brynn Brower**: investigation, writing – review and editing, validation, visualization, methodology, formal analysis, data curation. **Venkatraman Gopalan**: conceptualization, funding acquisition, writing – review and editing, validation, project administration, supervision, resources. **Tobias Schwaigert**: investigation, validation, writing – review and editing. **Suchismita Sarker**: funding acquisition, resources, methodology. **Darrell G. Schlom**: supervision, resources, project administration, writing – review and editing, methodology, funding acquisition, investigation.

Acknowledgements

S. H. and V. G. acknowledge support from the National Science Foundation grant DMREF-2522897 for thin film synthesis, electro-optic measurements, SHG measurements, x-ray experiments, and manuscript preparation. V. G. acknowledges support for electro-optic measurement equipment from the Materials Research Institute at Penn State. A. R., L. Q. C., and V. G. acknowledge support from the National Science Foundation grant DMREF-2522897 for the phase-field simulations. A. R. and I. R. P. acknowledges the support of the National Science Foundation Graduate Research Fellowship Program under Grant Number DGE1255832. The phase-field simulations in this work were conducted with the advanced computing resources provided by Texas A&M High Performance Research Computing, through allocation MAT250123 from the ACCESS program, which is supported by National Science Foundation Grants Nos. 2138259, 2138286, 2138307, 2137603, and 2138296. B. B. and I. R. P. acknowledge support from the National Science Foundation grant DMREF-2522897 for partial electro-optic measurements and manuscript preparation. M.A.H.C. acknowledges support from the National Science Foundation grant DMREF-2522897 for sample preparation and waveguide simulations. The $KNbO_3$ thin films were synthesized at the Platform for the Accelerated Realization, Analysis, and Discovery of Interface Materials (PARADIM), which is supported by the National Science Foundation (NSF) under Cooperative Agreement No. DMR-2039380. T. S. and D. G. S. acknowledge support from the NSF through PARADIM under Cooperative Agreement No. DMR-2039380. A. S. and V. G. acknowledge support from the Center for 3D Ferroelectric Microelectronics and Manufacturing ($3DFeM_2$), an Energy Frontier Research Center funded by the U.S. Department of Energy, Office of Science, Office of Basic Energy Sciences Energy Frontier Research Centers program under Award Number DE-SC0021118, for partial electro-optic measurements. This work is based on research conducted at the Center for High-Energy X-ray Sciences (CHEXS), which is supported by the National Science Foundation (BIO, ENG and MPS Directorates) under award DMR-2342336. [Correction added on October 29, 2026, after first online publication: Acknowledgement Section in the article has been updated in this version.]

Conflicts of Interest

The authors have a provisional patent filed on this work. Long-Qing Chen has a financial interest in MuPRO, LLC, a company which licenses and markets the software package used in this research.

Data Availability Statement

The data that supports the findings of this study are available within the article. Datasets used for the generation of figures presented in the article is available at 10.6084/m9.figshare.32443038.

References

1. *Nonlinear Optics* (Elsevier, 2020).

2. L. Torrijos-Morán and D. Pérez-López, "Industry Insight: Photonics to Scale AI Data Centers," *npj Nanophotonics* 3 (2026): 8, https://doi.org/10.1038/s44310-025-00105-1.

3. R. Chen, Y. Wu, K. Zhang, et al., "Integrated Bionic LiDAR for Adaptive 4D Machine Vision," *Nature Communications* 17 (2025): 24, https://doi.org/10.1038/s41467-025-66529-7.

4. K. Alexander, A. Benyamini, D. Black, et al., "A Manufacturable Platform for Photonic Quantum Computing," *Nature* 641 (2025): 876.

5. Y. Wen, H. Chen, Z. Wu, W. Li, and Y. Zhang, "Fabrication and Photonic Applications of Si-Integrated $LiNbO_3$ and $BaTiO_3$ Ferroelectric Thin Films," *APL Materials* 12 (2024): 020601, https://doi.org/10.1063/5.0192018.

6. A. Boes, L. Chang, C. Langrock, et al., "Lithium Niobate Photonics: Unlocking the Electromagnetic Spectrum," *Science* 2023 (1979): 379, https://doi.org/10.1126/science.abj4396.

7. F. Eltes, G. E. Villarreal-Garcia, D. Caimi, et al., "An Integrated Optical Modulator Operating at Cryogenic Temperatures," *Nature Materials* 19 (2020): 1164–1168, https://doi.org/10.1038/s41563-020-0725-5.

8. A. Suceava, S. Hazra, A. Ross, et al., "Colossal Cryogenic Electro-Optic Response Through Metastability in Strained $BaTiO_3$ Thin Films," *Advanced Materials* 38, no. 3 (2026): e07564, https://doi.org/10.1002/adma.202507564.

9. H. Fu and R. E. Cohen, "Polarization Rotation Mechanism for Ultrahigh Electromechanical Response in Single-Crystal Piezoelectrics," *Nature* 403 (2000): 281–283, https://doi.org/10.1038/35002022.

10. H. Liu, J. Chen, L. Fan, et al., "Critical Role of Monoclinic Polarization Rotation in High-Performance Perovskite Piezoelectric Materials," *Physical Review Letters* 119 (2017): 017601, https://doi.org/10.1103/PhysRevLett.119.017601.

11. D. Chelladurai, M. Kohli, J. Winiger, et al., "Barium Titanate and Lithium Niobate Permittivity and Pockels Coefficients From Megahertz to Sub-Terahertz Frequencies," *Nature Materials* 24 (2025): 868–875, https://doi.org/10.1038/s41563-025-02158-1.

12. M. Zgonik, R. Schlesser, I. Biaggio, and P. Günter, "Electro-and Acousto-Optic Properties of $KNbO_3$ Crystals," *Ferroelectrics* 158 (1994): 217–222, https://doi.org/10.1080/00150199408216019.

13. L. Liang, Y. L. Li, L.-Q. Chen, S. Y. Hu, and G.-H. Lu, "Thermodynamics and Ferroelectric Properties of $KNbO_3$," *Journal of Applied Physics* 106 (2009): 104118, https://doi.org/10.1063/1.3260242.

14. S. Hazra, T. Schwaigert, A. Ross, et al., "Colossal Strain Tuning of Ferroelectric Transitions in $KNbO_3$ Thin Films," *Advanced Materials* 36 (2024): 2408664, https://doi.org/10.1002/adma.202408664.

15. S. A. Denev, T. T. A. Lummen, E. Barnes, A. Kumar, and V. Gopalan, "Probing Ferroelectrics Using Optical Second Harmonic Generation," *Journal of the American Ceramic Society* 94 (2011): 2699–2727, https://doi.org/10.1111/j.1551-2916.2011.04740.x.

16163028, 0, Downloaded from https://advanced.onlinelibrary.wiley.com/doi/10.1002/adfm.79070, Wiley Online Library on [16/11/2026]. See the Terms and Conditions (https://onlinelibrary.wiley.com/terms-and-conditions) on Wiley Online Library for rules of use; OA articles are governed by the applicable Creative Commons License

16. M. Segatto, D. Lizzit, and D. Esseni, "An LGD Model With Extrinsic Nucleations for Polarization Dynamics in Ferroelectric Materials and Devices," *Scientific Reports* 15 (2025): 19619, https://doi.org/10.1038/s41598-025-03469-8.

17. S. Kim, V. Gopalan, and A. Gruverman, "Coercive Fields in Ferroelectrics: A Case Study in Lithium Niobate and Lithium Tantalate," *Applied Physics Letters* 80 (2002): 2740–2742, https://doi.org/10.1063/1.1470247.

18. S. Ducharme, V. M. Fridkin, A. V. Bune, et al., "Intrinsic Ferroelectric Coercive Field," *Physical Review Letters* 84 (2000): 175–178, https://doi.org/10.1103/PhysRevLett.84.175.

19. S. Abel, T. Stöferle, C. Marchiori, et al., "A Strong Electro-Optically Active Lead-Free Ferroelectric Integrated on Silicon," *Nature Communications* 4 (2013): 1671, https://doi.org/10.1038/ncomms2695.

20. M. Aillerie, N. Théofanous, and M. D. Fontana, "Measurement of the Electro-Optic Coefficients: Description and Comparison of the Experimental Techniques," *Applied Physics B: Lasers and Optics* 70 (2000): 317–334, https://doi.org/10.1007/s003400050053.

21. X. Yuan, Y. Sakurai, S. Kondo, M. Yoshino, T. Nagasaki, and T. Yamada, "Effect of Ni Doping on the Electro-Optic Property in K $(Ta_{0.6}Nb_{0.4})O_3$ Films," *Japanese Journal of Applied Physics* 61 (2022): SN1005.

22. S. Kondo, R. Shimura, T. Teranishi, et al., "Linear Electro-Optic Effect in Ferroelectric HfO_2 -Based Epitaxial Thin Films," *Japanese Journal of Applied Physics* 60 (2021): 070905, https://doi.org/10.35848/1347-4065/ac087d.

23. S. Kondo, T. Yamada, A. K. Tagantsev, et al., "Large Impact of Strain on the Electro-Optic Effect in (Ba, Sr)TiO_3 Thin Films: Experiment and Theoretical Comparison," *Applied Physics Letters* 115 (2019): 092901, https://doi.org/10.1063/1.5117218.

24. Y. Wen, Y. Cao, H. Chen, et al., "Enhanced Electro-Optic Coefficients in Single-Crystalline $BaTiO_3$ Thin Films Enabled by Domain Alignment," *Advanced Optical Materials* 12 (2024): 2303058, https://doi.org/10.1002/adom.202303058.

25. Y. Cao, Y. Wen, Y. Yang, et al., "Low-Temperature Growth of Epitaxial $BaTiO_3$ Thin Films With Significant Electro-Optic Coefficients," *Applied Physics Letters* 126 (2025): 111104, https://doi.org/10.1063/5.0237644.

26. X. Yuan, T. Yamada, and L. Meng, "Strong Electro-Optic Effect in Mg Incorporated ZnO Thin Films," *Applied Physics Letters* 121 (2022): 152903, https://doi.org/10.1063/5.0103831.

27. K. J. Kormondy, S. Abel, F. Fallegger, et al., "Analysis of the Pockels Effect in Ferroelectric Barium Titanate Thin Films on Si(0 0 1)," *Microelectronic Engineering* 147 (2015): 215–218, https://doi.org/10.1016/j.mee.2015.04.041.

28. H. Yu, N. Guo, C. Deng, et al., "Tuning the Electro-Optic Properties of $BaTiO_3$ Epitaxial Thin Films via Buffer Layer-Controlled Polarization Rotation Paths," *Advanced Functional Materials* 34 (2024): 2315579, https://doi.org/10.1002/adfm.202315579.

29. M. Sun, C. Zheng, Y. Gao, et al., "Linear Electro-Optic Modulation in Highly Polarizable Organic Perovskites," *Advanced Materials* 33 (2021): 2006368, https://doi.org/10.1002/adma.202006368.

30. Y. Gao, G. Walters, Y. Qin, et al., "Electro-Optic Modulation in Hybrid Metal Halide Perovskites," *Advanced Materials* 31 (2019): 1808336, https://doi.org/10.1002/adma.201808336.

31. A. Ross, M. S. M. M. Ali, A. Saha, et al., "Thermodynamic Theory of Linear Optical and Electro-Optical Properties of Ferroelectrics," *Physical Review B* 111 (2025): 085109, https://doi.org/10.1103/PhysRevB.111.085109.

32. A. Ross, V. Gopalan, and L.-Q. Chen, "Thermodynamics of Ferroelectric and Optical Properties in $KNbO_3$," preprint, ArXiv, January 23, 2026, https://doi.org/10.48550/arXiv.2601.17150.

33. H. Akamatsu, Y. Yuan, V. A. Stoica, et al., "Light-Activated Gigahertz Ferroelectric Domain Dynamics," *Physical Review Letters* 120 (2018): 096101, https://doi.org/10.1103/PhysRevLett.120.096101.

34. X. Li, A. Ross, and V. A. Stoica, "Decoding THz-Driven Dynamic Fingerprints of Ferroelectric Nanotwin Networks," *Advanced Materials* 38 (2026): 73118, https://doi.org/10.1002/adma.73118.

35. Q. Li, V. A. Stoica, M. Paściak, et al., "Subterahertz Collective Dynamics of Polar Vortices," *Nature* 592 (2021): 376–380, https://doi.org/10.1038/s41586-021-03342-4.

36. R. Mankowsky, A. von Hoegen, M. Först, and A. Cavalleri, "Ultrafast Reversal of the Ferroelectric Polarization," *Physical Review Letters* 118 (2017): 197601, https://doi.org/10.1103/PhysRevLett.118.197601.

37. X. Li, T. Qiu, J. Zhang, et al., "Terahertz Field–Induced Ferroelectricity in Quantum Paraelectric SrTiO3," *Science* 364 (2019): 1079–1082.

38. J. Shi, C. Heide, H. Xu, et al., "Nonresonant Raman Control of Ferroelectric Polarization," *Advanced Materials* 37 (2025): 10524, https://doi.org/10.1002/adma.202510524.

39. C. Wang, M. Zhang, X. Chen, et al., "Integrated Lithium Niobate Electro-Optic Modulators Operating at CMOS-Compatible Voltages," *Nature* 562 (2018): 101–104, https://doi.org/10.1038/s41586-018-0551-y.

40. J. Zhao, M. Ahmadi, B. Noheda, and M. F. Sarott, "Integration of Imprint-Free and Low Coercivity Ferroelectric $BaTiO_3$ Thin Films on Silicon," *Nano Letters* 26 (2026): 764–772, https://doi.org/10.1021/acs.nanolett.5c05139.

41. S. Ismail-Beigi, F. J. Walker, S.-W. Cheong, K. M. Rabe, and C. H. Ahn, "Alkaline Earth Stannates: The Next Silicon?," *APL Materials* 3 (2015): 062510.

42. H. Li, J. Finder, Y. Liang, R. Gregory, and W. Qin, "Dielectric Properties of Epitaxial $Ba_{0.5}Sr_{0.5}TiO_3$ Films on Amorphous SiO_2 on Sapphire," *Applied Physics Letters* 87 (2005): 072905, https://doi.org/10.1063/1.2011774.

43. V. Vaithyanathan, J. Lettieri, W. Tian, et al., "c -Axis Oriented Epitaxial $BaTiO_3$ Films on (001) Si," *Journal of Applied Physics* 100 (2006): 024108, https://doi.org/10.1063/1.2203208.

44. B. Wang, H.-N. Chen, J.-J. Wang, and L.-Q. Chen, "Ferroelectric Domain Structures and Temperature-Misfit Strain Phase Diagrams of $K_{1-x}Na_xNbO_3$ Thin Films: A Phase-Field Study," *Applied Physics Letters* 115 (2019): 092902, https://doi.org/10.1063/1.5116910.

45. M.-H. M. Hsu, A. Marinelli, C. Merckling, et al., "Orientation-Dependent Electro-Optical Response of $BaTiO_3$ on $SrTiO_3$-Buffered Si(001) Studied via Spectroscopic Ellipsometry," *Optical Materials Express* 7 (2017): 2030, https://doi.org/10.1364/OME.7.002030.

46. C.-A. Berseth, C. Wuethrich, and F. K. Reinhart, "The Electro-Optic Coefficients of GaAs: Measurements at 1.32 and 1.52 μm and Study of Their Dispersion Between 0.9 and 10 μm," *Journal of Applied Physics* 71 (1992): 2821–2825, https://doi.org/10.1063/1.351011.

47. D. B. Chenault, R. A. Chipman, and S.-Y. Lu, "Electro-Optic Coefficient Spectrum of Cadmium Telluride," *Applied Optics* 33 (1994): 7382, https://doi.org/10.1364/AO.33.007382.

48. M. Zhu, Z. Du, L. Jing, A. I. Yoong Tok, and E. H. Tong Teo, "Optical and Electro-Optic Anisotropy of Epitaxial PZT Thin Films," *Applied Physics Letters* 107 (2015): 031907, https://doi.org/10.1063/1.4927404.

49. P. Rabiei and P. Gunter, "Optical and Electro-Optical Properties of Submicrometer Lithium Niobate Slab Waveguides Prepared by Crystal Ion Slicing and Wafer Bonding," *Applied Physics Letters* 85 (2004): 4603–4605, https://doi.org/10.1063/1.1819527.

50. Z. Sun, Z. Cui, M. Sun, et al., "Electro-Optic Coefficient Measurement of a $K(H_{1-x}D_x)_2PO_4$ Crystal Based on $\chi^{(2)}$ Nonlinear Optical Technology," *Optics Express* 29 (2021): 2647, https://doi.org/10.1364/OE.415262.

51. M. Zgonik, P. Bernasconi, M. Duelli, et al., "Dielectric, Elastic, Piezoelectric, Electro-Optic, and Elasto-Optic Tensors of $BaTiO_3$ crystals,"

16163028, 0, Downloaded from https://advanced.onlinelibrary.wiley.com/doi/10.1002/adfm.79070, Wiley Online Library on [16/11/2026]. See the Terms and Conditions (https://onlinelibrary.wiley.com/terms-and-conditions) on Wiley Online Library for rules of use; OA articles are governed by the applicable Creative Commons License

Physical Review B 50 (1994): 5941–5949, https://doi.org/10.1103/PhysRevB.50.5941.

52. K. M. Adkison, S.-L. Shang, B. J. Bocklund, D. Klimm, D. G. Schlom, and Z.-K. Liu, "Suitability of Binary Oxides for Molecular-Beam Epitaxy Source Materials: A Comprehensive Thermodynamic Analysis," *APL Materials* 8 (2020): 081110, https://doi.org/10.1063/5.0013159.

53. H. Okamoto, "In-K (Indium-Potassium)," *Journal of Phase Equilibria* 13 (1992): 217–218, https://doi.org/10.1007/BF02667497.

54. R. E. Honig and D. A. Kramer, *Vapor Pressure Data for the Solid and Liquid Elements* (RCA Laboratories, David Sarnoff Research Center, 1969).

55. T. Schwaigert, S. Salmani-Rezaie, M. R. Barone, et al., "Molecular Beam Epitaxy of $KTaO_3$," *Journal of Vacuum Science & Technology A* 41 (2023): 022703, https://doi.org/10.1116/6.0002223.

56. Y. L. Li, S. Y. Hu, Z. K. Liu, and L. Q. Chen, "Effect of Substrate Constraint on the Stability and Evolution of Ferroelectric Domain Structures in Thin Films," *Acta Materialia* 50 (2002): 395–411, https://doi.org/10.1016/S1359-6454(01)00360-3.

Supporting Information

Additional supporting information can be found online in the Supporting Information section.

Supporting File 1: adfm79070-sup-0001-SuppMat.docx.

Supporting File 2: adfm79070-sup-0002-VideoS1.mp4.

Supporting File 3: adfm79070-sup-0003-VideoS2.avi.

Supporting File 4: adfm79070-sup-0004-VideoS3.avi.

Supporting File 5: adfm79070-sup-0005-VideoS4.mp4.

16163028, 0, Downloaded from https://advanced.onlinelibrary.wiley.com/doi/10.1002/adfm.79070, Wiley Online Library on [16/11/2026]. See the Terms and Conditions (https://onlinelibrary.wiley.com/terms-and-conditions) on Wiley Online Library for rules of use; OA articles are governed by the applicable Creative Commons License

Supporting Information

Exceptional Electro-Optic Coefficient Unlocked via Polarization Swaying in $KNbO_3$ Thin Films

*Sankalpa Hazra, Aiden Ross, Brynn Brower, Tobias Schwaigert, Ian Reed Philippi, Albert Suceava, Himirkanti Sarkar, Muhammed Aminul Haque Choudhury, Suchismita Sarker, Darrell G. Schlom, Long-Qing Chen, and Venkatraman Gopalan**

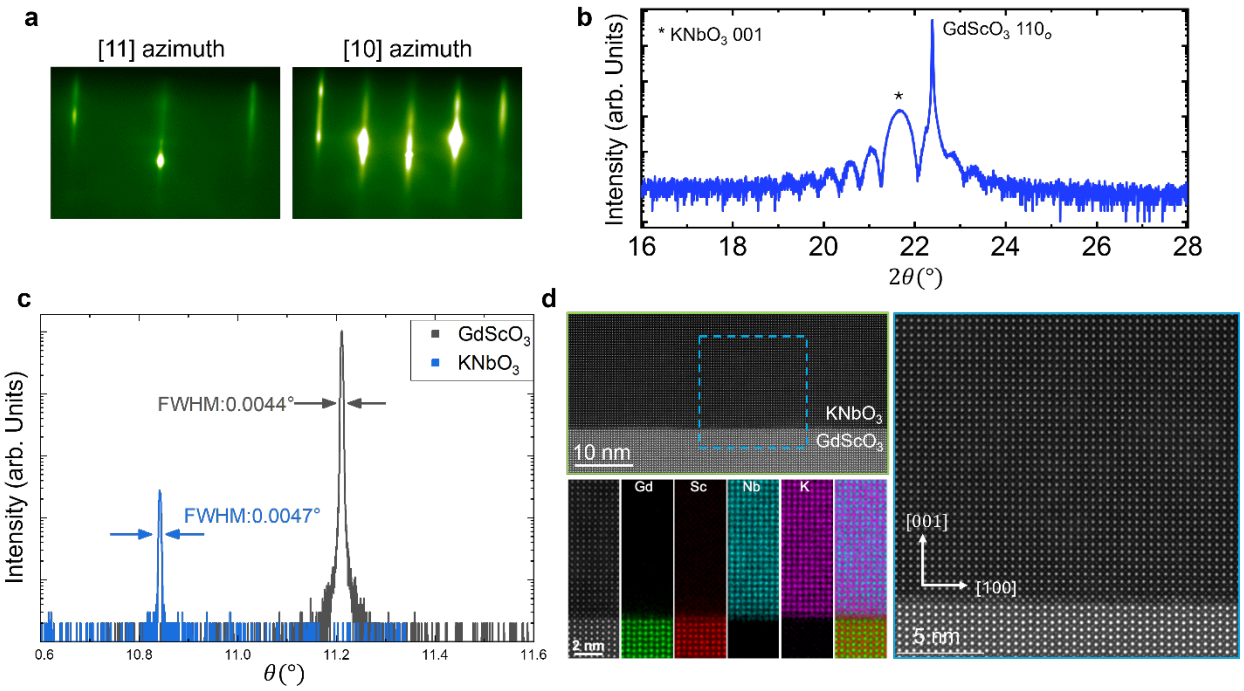


Figure S1: a) Reflection high-energy electron diffraction of $KNbO_3$ film grown on $GdScO_3$ along the [11] and [10] azimuth, taken after growth confirming a smooth surface structure. **b)** $\theta - 2\theta$ XRD scan of the $KNbO_3$ film grown on $GdScO_3$, exhibiting Laue fringes indicating a sharp interface between film and substrate. **c)** Lab x-ray based overlaid rocking curves around the 001 $KNbO_3$ peak compared to 110_o $GdScO_3$ substrate. Subscript "o" refers to the orthorhombic unit cell of the $GdScO_3$ substrate. The rocking curves are measured along the $[\bar{1}10]_o$ direction of the $GdScO_3$ substrate. **d)** Cross-sectional transmission electron microscopy images of $KNbO_3$ thin film grown on $GdScO_3$ substrate. The interface structure is uniform throughout the sample, indicating a coherently strained film growth. The atomic resolution EDX map reveals an intermixing of metal ions at the interface, primarily involving scandium from the substrate and niobium from the film. This intermixed layer is crucial for maintaining charge neutrality at the KO terminating layer. The absence of defects and the coherent strain between the $KNbO_3$ film and the $GdScO_3$ substrate indicate the high quality of epitaxial growth. Further details of thin film synthesis and characterization is elaborated elsewhere[1].

Note 1: Second-Harmonic Generation measurements

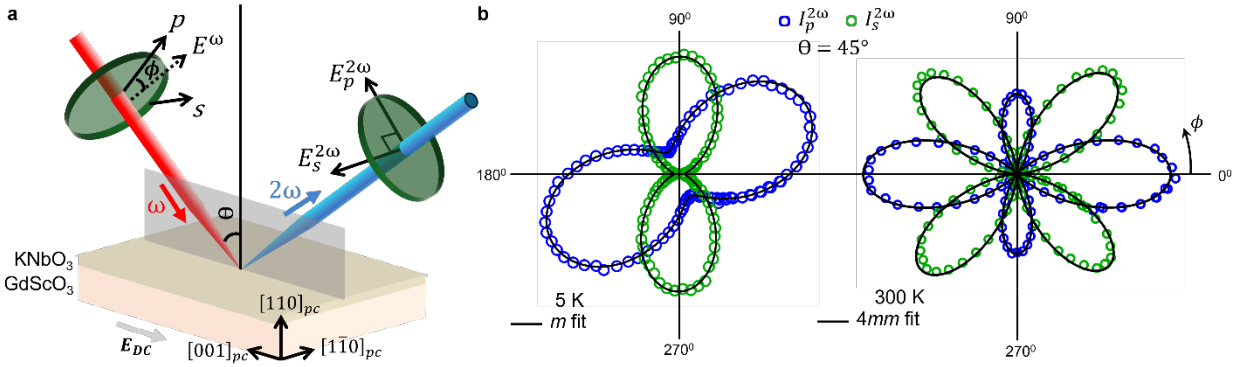


Figure S2: a) Schematic of the SHG setup used for measurements. **b)** Oblique incidence SHG polarimetry taken at 5 K and 300 K fitted to a multi-domain monoclinic (point group m) and single-domain tetragonal (point group $4mm$) models respectively.

Electric dipole second-harmonic generation (SHG) is a nonlinear optical process which converts fundamental light at ω frequency into second-harmonic light at twice the frequency (2ω) reflected off the sample.[2] A schematic of the setup used for measurements is shown in **Figure S2a**. By rotating the polarization of the incident fundamental light (ϕ), polar plots can be generated corresponding to the two orthogonal polarizations of the measured SHG (p and s-polarized) signal. By fitting the SHG polar plots, the point group symmetry of a material can be determined.

Figure S2b shows the measured SHG polar plots of $KNbO_3$ on $GdScO_3$ at an oblique incidence ($\theta = 45°$) of the fundamental light. While the room temperature polar plot can be fitted to a tetragonal model (point group $4mm$), a multidomain monoclinic model (point group m) is necessary to fit the SHG polar plots at 5 K.[1] This is consistent with the observed tetragonal-to-monoclinic phase transition in $KNbO_3$ on $GdScO_3$.

In lab coordinates (X, Y, Z), the electric field of the incident beam can be written as $(E_o \cos\phi,\ E_o sin\ \phi, 0)$ where ϕ is the polarization rotation angle introduced by the half wave plate as shown in **Figure S2a**. Here, $X \,||\, p, Y \,||\, z$ and Z is along the direction of the fundamental beam. For an incidence angle θ on the sample, the electric field in the crystal axes coordinates can be expressed as $(E_o \cos\varphi \cos\theta, E_o \sin\varphi, -E_o \cos\varphi \sin\varphi)$. The induced nonlinear polarization $P^{2\omega}$, is related to the incident electric field through the nonlinear susceptibility tensor, d_{ijk} through the following equation:

$$P_i^{2\omega} \propto d_{ijk} E_j^{\omega} E_k^{\omega} \qquad (1)$$

The proportionality constants depend on incident beam fluence, Fresnel's coefficients at the film-air and film-substrate interfaces and the thickness of the films.

Tetragonal model:

For tetragonal unit cell the nonlinear susceptibility can be written in Voigt notation as:

$$\begin{pmatrix} 0 & 0 & 0 & 0 & d_{15} & 0 \\ 0 & 0 & 0 & d_{15} & 0 & 0 \\ d_{31} & d_{31} & d_{33} & 0 & 0 & 0 \end{pmatrix}$$

The induced nonlinear polarization in the crystal coordinates i = (1,2,3) (calculated through equation 1) can be rotated back to lab coordinates (X, Y, Z), to give the p and s-polarized components of the SHG (p || X and s || Y). The p and s-polarized SHG intensities can be expressed as follows:

For normal incidence ($\theta = 0°$):

$$I_p^{2\omega} \propto \left(P_p^{2\omega}\right)^2 = 0 \tag{2}$$

$$I_s^{2\omega} \propto (P_s^{2\omega})^2 = 0$$

For oblique incidence ($\theta = 45°$):

$$I_p^{2\omega} \propto \left(P_p^{2\omega}\right)^2 \propto ((2d_{15} - d_{31} - d_{33})cos[\varphi]^2 - 2d_{31}sin[\varphi]^2)^2 \tag{3}$$

$$I_s^{2\omega} \propto (P_s^{2\omega})^2 \propto d_{15}^2 Sin[2\varphi]^2$$

Figure S2b shows the SHG polar plots of $KNbO_3$ on $GdScO_3$ at 300K fitted to a tetragonal model.

Monoclinic model:

For the low temperature monoclinic phase (point group m) in $KNbO_3$, a multi-domain model is used. In crystal physics coordinates i = (1, 2, 3), nonlinear susceptibility in the monoclinic phase can be written as:

$$d_{ij} = \begin{pmatrix} d_{11} & d_{12} & d_{13} & 0 & d_{15} & 0 \\ 0 & 0 & 0 & d_{24} & 0 & d_{26} \\ d_{31} & d_{32} & d_{33} & 0 & d_{35} & 0 \end{pmatrix}$$

Here, the monoclinic mirror plane is perpendicular to the crystallographic *b*-axis of the monoclinic cell of $KNbO_3$ which is parallel to *i*=2 crystal physics coordinate. Through rotating the unit cell by right angles, 4 such unit cells can be achieved, each associated with an area fraction labelled as below:

Domain 1: *a* || 1, *b* || 2, *c* || 3 (Area fraction: A_1)

Domain 2: *a* || 2, *b* || -1, *c* || 3 (Area fraction: A_2)

Domain 3: *a* || -1, *b* || -2, *c* || 3 (Area fraction: A_3)

Domain 4: *a* || -2, *b* || 1, *c* || 3 (Area fraction: A_4)

Here (*a*, *b*, *c*) denote the crystallographic axes of the monoclinic unit cell, *i* = (1,2,3) denote the previously defined crystal physics coordinate system and the area fractions are constrained to $A_1 + A_2 + A_3 + A_4 = 1$.

For normal incidence ($\theta = 0°$):

From Equation 1, the induced nonlinear polarization can be calculated in the crystal coordinate system and can be transformed into lab coordinates (X, Y, Z). The resultant nonlinear polarization in the lab coordinates X (*p*-polarized) and Y (*s*-polarized) are tabulated below (**Table S1**):

Table S1: *p* and *s*-polarization components for different domains

	$P_p^{2\omega}$	$P_s^{2\omega}$
Domain 1	$d_{11}cos^2\varphi + d_{12}sin^2\varphi$	$d_{26}sin\,2\varphi$
Domain 2	$d_{26}sin\,2\varphi$	$d_{12}cos^2\varphi + d_{11}sin^2\varphi$
Domain 3	$-(d_{11}cos^2\varphi + d_{12}sin^2\varphi)$	$-d_{26}sin\,2\varphi$
Domain 4	$-d_{26}sin\,2\varphi$	$-(d_{12}cos^2\varphi + d_{11}sin^2\varphi)$

The effective SHG intensity can be calculated as follows:

$$I_p^{2\omega} \propto \left(P_p^{2\omega}\right)^2 \propto \left(A_1 P_{p,domain\,1}^{2\omega} + A_2 P_{p,domain\,2}^{2\omega} + A_3 P_{p,domain\,3}^{2\omega} + A_4 P_{p,domain\,4}^{2\omega}\right)^2$$

This can be simplified to:

$$I_p^{2\omega} \propto K_{1p}\left(sin^2\,\varphi + K_{2p}cos^2\,\varphi\right)^2 + K_{3p}sin^2\,2\varphi + K_{4p}\left(sin^2\,\varphi + K_{2p}cos^2\,\varphi\right)sin\,2\varphi \quad (4)$$

where,

$$K_{1p} = \delta A_1^2 d_{12}^2\; K_{2p} = \frac{d_{11}}{d_{12}}\; K_{3p} = \delta A_2^2 d_{26}^2\; K_{4p} = 2\delta A_1 \delta A_2 d_{12} d_{26}$$

$\delta A_1 = A_1 - A_3$ and $\delta A_2 = A_2 - A_4$. Similar expressions can also be derived for $I_s^{2\omega}$ with the following coefficients:

$$K_{1s} = \delta A_2^2 d_{11}^2\; K_{2s} = \frac{d_{12}}{d_{11}}\; K_{3s} = \delta A_1^2 d_{26}^2\; K_{4s} = 2\delta A_1 \delta A_2 d_{11} d_{26}$$

For oblique incidence ($\theta = 45°$):

Equations for oblique incidence polarimetry involve more convoluted combinations of *d*-coefficients and area fractions, however they can be reduced to the same form as equation (4). The exact convolutions are listed below:

$$K_{1p} = \frac{1}{8}[2(A_1 + A_3)d_{32} + 2\delta A_1 d_{12} + 2d_{31}(A_2 + A_4)]^2$$

$$K_{2p} = \frac{1}{2\sqrt{2K_{1p}}}[\delta A_1(d_{11} + d_{13} - 2d_{35}) + (A_1 + A_3)(d_{31} + d_{33} - 2d_{15}) + (A_2 + A_4)(d_{32} + d_{33} - 2d_{24}]$$

$$K_{3p} = \frac{[\delta A_2(d_{26} - d_{35})]^2}{4}$$

$$K_{4p} = 2\sqrt{K_{1p}K_{3p}}$$

$$K_{1s} = \frac{1}{4}(A_2 - A_4)^2 d_{11}^2$$

$$K_{2s} = \frac{1}{2\sqrt{K_{1s}}}(d_{12} + d_{13})(A_2 - A_4)$$

$$K_{3s} = \frac{1}{4}\left(\sqrt{2}A_1(d_{26} - d_{24}) - \sqrt{2}A_3(d_{26} + d_{24}) + \frac{d_{15}}{\sqrt{2}}(A_4 - A_2)\right)^2$$

$$K_{4s} = 2\sqrt{K_{1s}K_{3s}}$$

Temperature dependent SHG measurements in normal incidence

As described in equations 2 and 4, at normal incidence no SHG signal can be observed in the tetragonal phase, but a finite response is measurable in the monoclinic phase. **Main text, Figure 1b**, shows the temperature evolution of the normal incidence SHG response of compressively strained $KNbO_3$ on $GdScO_3$ showing a finite SHG response below 275 K marking the tetragonal-to-monoclinic phase transition.

Electric-field dependent SHG measurements in oblique incidence

To probe the electric-field driven switching of the monoclinic polarization, SHG measurements were performed at oblique incidence with an in-plane electric field applied along the $[001]_{pc}$ direction of the $GdScO_3$ substrate (**Figure S2a**). The p-polarized SHG intensity was used for measurements with the polarization of the fundamental light set to lie along the X-direction in the laboratory frame of reference $I_p^{2\omega}(\phi = 0°)$.

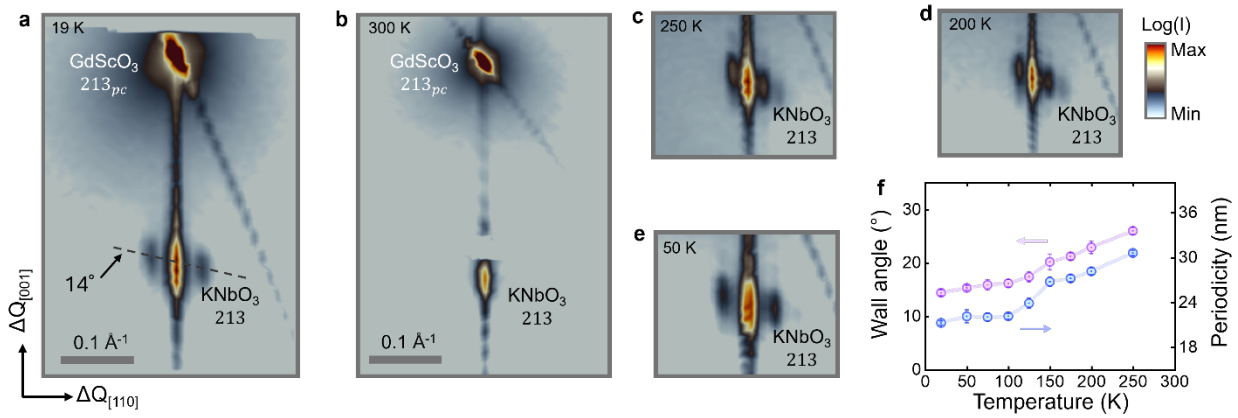


Figure S3: a) Reciprocal space map (RSM) around the $GdScO_3$ 213_{pc} peak at 19 K confirming coherently strained $KNbO_3$ film. Tilted diffused satellites around the film peak correlate with tilted domain walls between monoclinic domains (elaborated elsewhere)[1,3]. The tilted satellite peak arrangement is proxy for the monoclinic phase observation. **b)** RSM around $GdScO_3$ 213_{pc} substrate peak at 300 K showing no diffused satellite patterns around the film peak. This is expected for the tetragonal phase of $KNbO_3$ at 300 K. **c)** Zoomed-in RSM around the $KNbO_3$ 213 film peak demonstrating tilted domain patterns below 275 (tetragonal-to-monoclinic) phase transition temperature. **d)** Zoomed-in RSM around the $KNbO_3$ 213 peak at 200 K. **e)** Zoomed-in RSM around the $KNbO_3$ 213 peak at 50 K. **f)** Variation of domain wall angle tilt (measured from the in-plane direction in the monoclinic phase (<275 K). Temperature variation of the monoclinic domain wall periodicity along the [110] direction. Error bars are calculated by averaging across several measured peaks.

Note 2: Beam propagation and derivation of $n_e(\theta_{film})$ from spectroscopic ellipsometry

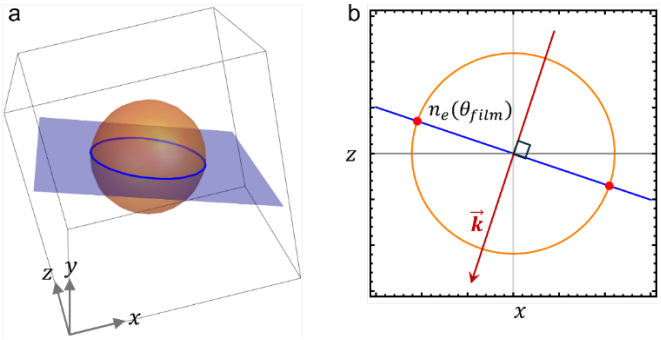


Figure S4: a) Index ellipsoid at zero field intersected by the plane normal to the propagating beam direction ($\vec{k}$). The resulting ellipse gives the semi-major axis of n_o and a semi-minor axis of $n_e(\theta_{film})$. **b)** xz-cut of the index ellipsoid showing $n_e(\theta_{film})$ indicated by the red points.

For our measurements the sample is orientated such that the crystal physics coordinate system (1,2,3) of both the tetragonal and monoclinic phases is aligned with the laboratory coordinate system (x, y, z), i.e. $x \parallel 1, y \parallel 2, z \parallel 3$. The index ellipsoid in the crystal physics axis coordinate system under no external field can be described as:

$$\frac{x^2}{n_1^2} + \frac{y^2}{n_2^2} + \frac{z^2}{n_3^2} = 1 \tag{5}$$

The z-axis (crystal physics 3 direction) represents the out-of-plane direction of the sample. For electro-optic measurements with an incident beam at a 45° angle, the refracted beam sees a reduced angle θ_{film} on account of Snell's law. For simplicity, only the propagating angle for the ordinary ray ($\theta_{film} \sim 18°$) from the normal is considered. Given this angle, one can formulate the equation of a plane describing the polarization states for this ray:

$$\vec{p} = \{\cos\theta_{film}, 0, \sin\theta_{film}\} \qquad \vec{s} = \{0,1,0\} \tag{6}$$
$$\vec{n} = \vec{p} \times \vec{s}$$
$$n_x x + n_y y + n_z z = 0$$

The intersection of **Equation 6** with the index ellipsoid of **Equation 5** describes the cross-sectional ellipse whose perimeter describes the refractive indices experienced by the propagating ray (**Figure S4**). Under an applied electric field along crystal physics 1 direction the crystal physics 2 axis remains undisturbed ($2 = 2'$, $n_2 = n_2' = n_o$). Hence, we set $y = 0$ to view the cross-sectional of **Equation 6** and **Equation 5** in the xz plane only which reveals $n_e(\theta_{film})$. The experimentally measured Δn can be interpreted as $\Delta n = n_e(\theta_{film}) - n_e(\theta_{film})$, where $n_e(\theta_{film})'$ is the extraordinary refractive index of perturbed ellipsoid under an applied electric field.

Note 3: Extracting Δn vs E_{AC} from phase-field using a lock-in detection scheme

To derive a theory predicted S-curve, phase-field simulations of the optical dielectric susceptibility tensor (χ_{ij}) were performed with a sinusoidally varying electric field. Several simulations were performed by varying the peak of the applied sinusoidal electric field. For a particular simulation, the χ_{ij} tensor at every field was converted to its corresponding optical indicatrix tensor ($B_{ij} = \chi_{ij}^{-1}$) which was the used to construct the index ellipsoid according to:

$$B_{11}x^2 + B_{22}y^2 + B_{33}z^2 + 2B_{13}xz + 2B_{12}xy + 2B_{23}yz = 1 \quad (7)$$

As discussed in **Note 2**, the eigenvalues of the cross-sectional ellipse in the plane containing the beam propagation wave vector $\vec{\boldsymbol{k}}$ yields n_o (ordinary) and $n_e(\theta_{film})$ (extraordinary), where θ_{film} is the angle between $\vec{\boldsymbol{k}}$ and z, the angle made by the propagating beam with z direction.

The probe beam is incident at 45° to the sample surface normal. Applying Snell's law at the air–crystal interface,

$$sin\ \theta_{film} = \frac{sin(45°)}{n_o}$$

gives a refracted angle $\theta_{film} \approx 18.65°$ inside the material (for $n_o = 2.2117$). The refracted wave vector is

$$\vec{\boldsymbol{k}} = (sin\ \theta_{film}, 0, cos\ \theta_{film})$$

lying in the lying in the xz-plane (**Figure S4**). The cross-section of the indicatrix perpendicular to $\vec{\boldsymbol{k}}$ is an ellipse whose semi-axes yield n_o and $n_e(\theta_{film})$.

Using this formalism, simulated Δn ($= n_e'(\theta_{film}) - n_e(\theta_{film})$) is generated as a function of a sinusoidally varying electric field. To simulate the effect of a lock-in amplifier, first the frequency ω of the applied electric field is derived from the time domain fitting of the applied electric field. Next, the in-phase (X) and quadrature (Y) components are derived using:

$$X = \frac{2}{T}\int_0^T \Delta n(t) \cdot \sin(\omega t)dt, \quad Y = \frac{2}{T}\int_0^T \Delta n(t) \cdot \cos(\omega t)dt$$

It is important to ensure that the integral is performed only over one complete cycle of the electric field. The resultant simulated lock-in amplitude can be calculated via:

$$R = \sqrt{X^2 + Y^2}$$

The phase-field simulated Δn vs E_{AC} (**Main Text, Figure 2a, Figure S8**) is hence generated by calculating the lock-in amplitude corresponding to each simulation with a different amplitude of the sinusoidal electric field.

Note 4: Calculation of Electro-optic coefficient of $KNbO_3$ on $GdScO_3$

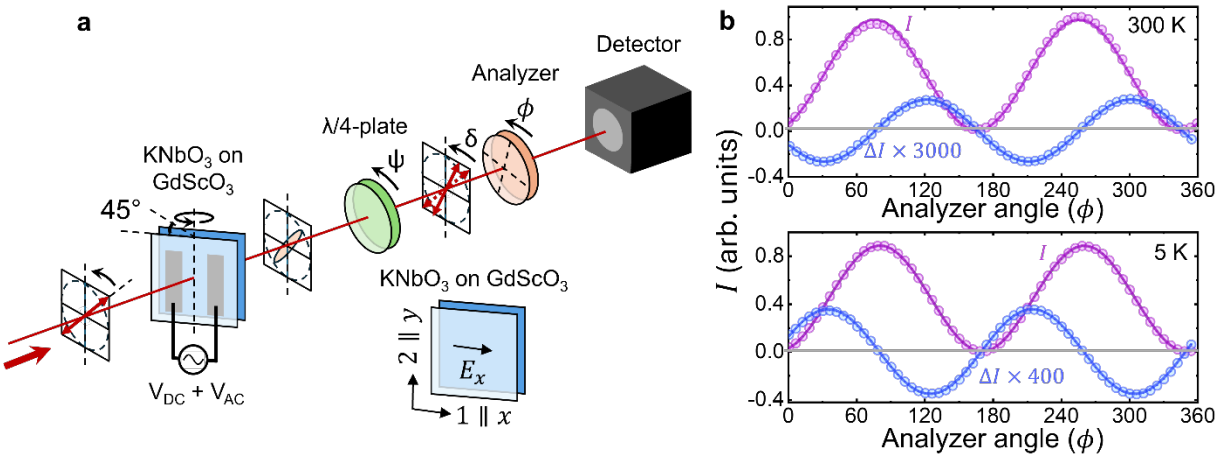


Figure S5: a) A schematic of the electro-optic setup used in experiments. Inset shows the orientational relationship between the crystal physics direction of the $KNbO_3$ film and the laboratory frame of reference. **b**) Unmodulated (I) and modulated (ΔI) as a function of analyzer angle measured in $KNbO_3$ on $GdScO_3$ at 5 K and 300 K confirming the electro-optic response. The modulated curves were measured using a $E_{AC} = 5$ kV cm^{-1}, and scaled for visibility.

Electro-optic measurements were performed using a polarizer-sample-compensator-analyzer (PSCA) setup[4–6]. In this method the change in transmission of light through a pair of crossed polarizers as a function of an applied electric to the sample is measured to quantify the field induced changed in refractive index. A schematic of the setup used for measurements is shown in **Figure S5a**. For the tetragonal phase of compressively strained $KNbO_3$ films the [001] crystallographic direction lies out-of-plane. The crystal physics 1, 2, and 3 directions are conveniently aligned with the crystallographic [100], [010], and [001] directions and are aligned with the laboratory axes (x, y, z). 500 μm square electrodes comprising of 150 nm Pt with a 5 nm Ti adhesion layer were deposited with 200 μm spacing to apply electric field along the [100] direction (**Figure S6**).

The incident polarization is set to lie between two principal optic axes of the sample, which in this study are the [100] and [010] in-plane crystallographic axes of the $KNbO_3$ film. The temperature dependent refractive indices of the $KNbO_3$ film were characterized using spectroscopic ellipsometry as shown in **Note 6**. With an in-plane electric field E_1 along the [100] crystallographic direction of $KNbO_3$ the index ellipsoid of the tetragonal phase distorts taking the original 1, 2, and 3 principal axes to a new set of axes: 1′, 2′ = 2, 3′:

$$\frac{x^2}{n_1^2} + \frac{y^2}{n_2^2} + \frac{z^2}{n_3^2} + 2xzr_{51}E_1 = 1 \qquad ()$$

In the absence of an external electric field, $x \equiv 1$, $y \equiv 2$, $z \equiv 3$ are the principal crystal physics axes, and with $n_1 = n_2 = n_o$ and $n_3 = n_e$ are the principle refractive indices. The action

of r_{51} would lead to new principal crystal coordinates in the $x-z$ plane, leading to $x' \equiv 1'$ and $z' \equiv 3'$ axes. The $y' \equiv 2' = y \equiv 2$ would remain unchanged under this field. The principal crystal coordinates and the refractive indices do not change in the $x-y$ plane as seen from equation 5. Hence, a normal incident probe would not sample any field induced change in refractive indices.

The sample is tilted 45° away from the incident probe direction as shown in **Figure R1**. The 1550 nm probe beam experiences two orthogonal refractive indices n_o and $n_e(\theta_{film})$ without any voltage applied to the sample, and $n_o{}' = n_o$ and $n_e'(\theta_{film})$ when external voltage is applied to the sample, where θ_{film} is the refracted angle of the probe beam inside the film. Even without an external electric field, the native birefringence induced by the sample changes the probe beam polarization from linear to an elliptical state. A quarter-wave plate after the sample cancels out this natural material birefringence, along with any birefringence induced by the different optical elements used in the setup. The final linear polarized light is measured via an analyzer.

The unmodulated probe beam (without an external electric field applied to the sample) is described by;

$$I = I_0 \cos^2(\phi + \delta) \tag{9}$$

where, ϕ represents the angle through which the analyzer is rotated and δ represents the overall phase accumulated by the probe beam transmission through the sample and other optical components as shown in **Figure R1.** Under an applied electric field the modulated intensity, ΔI, can be expressed as;

$$\Delta I = I_0 \, \Delta\delta \, \sin 2(\phi + \delta) \tag{10}$$

where, $\Delta\delta$, represents the change in phase acquired by the probe beam due to electric field induced change in refractive index of the sample. Assuming a single pass through the film, the measured $\Delta\delta$ can be related to the electric-field induced birefringence, $\Delta n = \frac{\Delta\delta\lambda}{2\pi L}$, where, $\lambda = 1550\, nm$ is the wavelength of the probe light used for measurements and $L = t/\cos(\theta_{film})$ is the path length of light travelled through the $KNbO_3$ film. The film thickness, t, is determined to be 37 nm from spectroscopic ellipsometry and x-ray reflectivity measurements. The electro-optic coefficient of the $KNbO_3$ film can now be extracted using equation (11), as follows;

$$r_{\text{eff}} = \frac{2\Delta n}{n_e(\theta_{\text{film}})^3 E_{AC}} \tag{11}$$

where, E_{AC}, is the applied electric field modulation.

Following **equation (9) and (10)**, maximum electric-field induced modulated probe intensity, ΔI, occurs at the half-way transmission point of the absolute unmodulated probe intensity, I, the point of maximum slope of I. The maximum of ΔI varies linearly with E_{AC} in the room temperature tetragonal phase, while in the low temperature monoclinic phase ΔI scales nonlinearly with a

multi-regime behavior as shown in **Main Text, Figure 2a**. The measured ΔI vs E_{AC} curves experimentally measured are first converted to Δn vs E_{AC} curves and slopes are taken at different regimes to enable extraction of the three different electro-optic coefficients, $r_{\mathrm{lf}}, r_{\mathrm{hf}}$ and r_{max}.

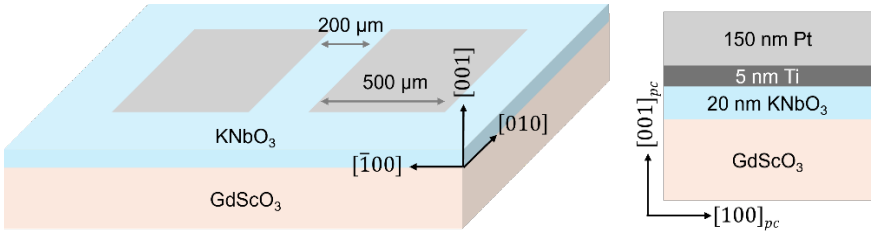


Figure S6: $500 \times 500\ \mu m^2$ electrodes with $200\ \mu m$ spacings are used for measurements. The electrodes constitute 5 nm Ti adhesion layer and a 150 nm thick Pt layer. Measurements are made with a beam size of 40 µm.

Note 5: Calibration of Electro-optic setup with standard LiNbO3 reference sample

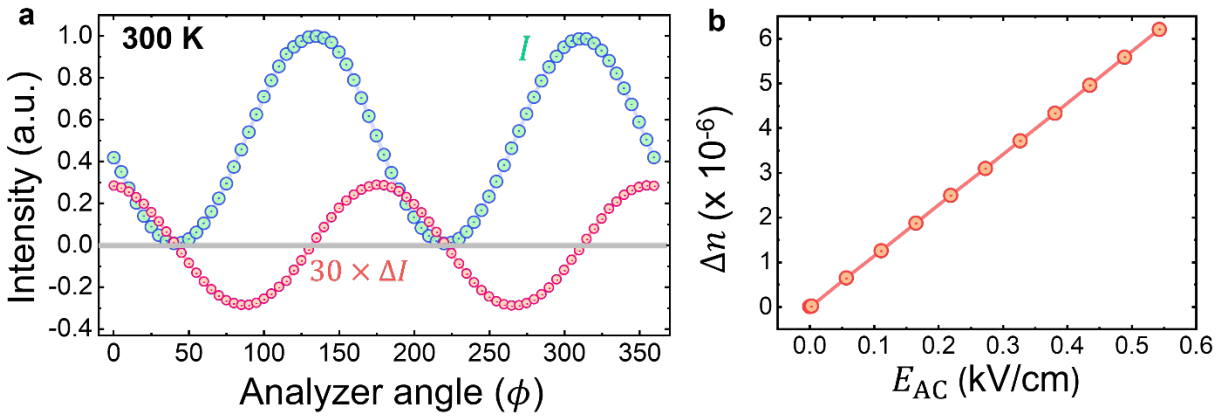


Figure S7: a) Unmodulated and Modulated intensity curves measured on an X-cut $LiNbO_3$ single crystal **b)** Experimentally measured change in refractive index change as a function of electric field applied showing a linear response.

Figure S7a shows electro-optic measurements on X-cut $LiNbO_3$ single crystal sample to benchmark the PSCA setup. Electric field was applied along the [0001] crystal axis (crystal physics 3 direction). The electrodes comprise of 100 nm Pt on both faces of the crystal to minimize fringing field effects which are relevant while measuring 0.5 mm thick single crystals. The gap between the electrodes was 1.85 mm and measurements were done at normal incidence.

A normal incidence measurement with field along the crystal physics 3 direction results in birefringence modulation owing to the r_{13} and r_{33} coefficients. Neither coefficients can be measured independently and hence an effective electro-optic response, $r_{\text{eff}} = r_{33} - \left(\frac{n_o^3}{n_e^3}\right) r_{13}$ is experimentally measured. From our experiments, $r_{eff} = 23.4$ pm/V (**Figure S7b**), in comparison to a predicted value of $r_{eff} = 21.3$ pm/V based on material parameters provided by MTI (supplier of the $LiNbO_3$ single crystal used for the experiment).

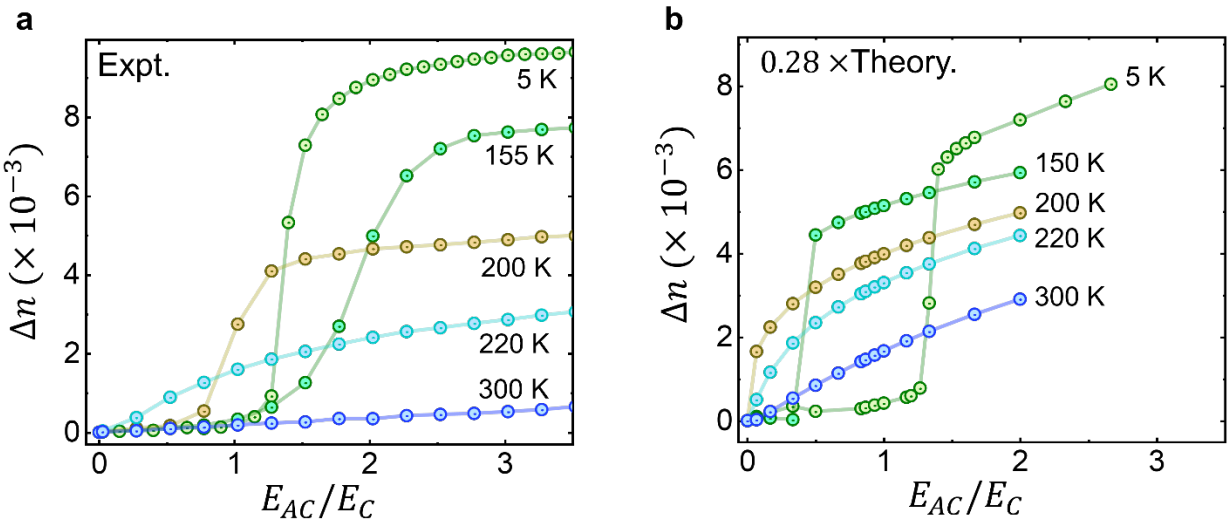


Figure S8: a) Experimentally measured Δn vs E_{AC}/E_C curves at various temperatures showing the evolution of the multi-regime response in the monoclinic phase (< 275 K). **b)** Phase-field simulated Δn vs E_{AC}/E_C curves at various temperatures. E_C is 1 for experiments and 30 for phase-field simulations.

Note 6: Linear optical properties of $KNbO_3$ on $GdScO_3$ from ellipsometry and UV-Vis

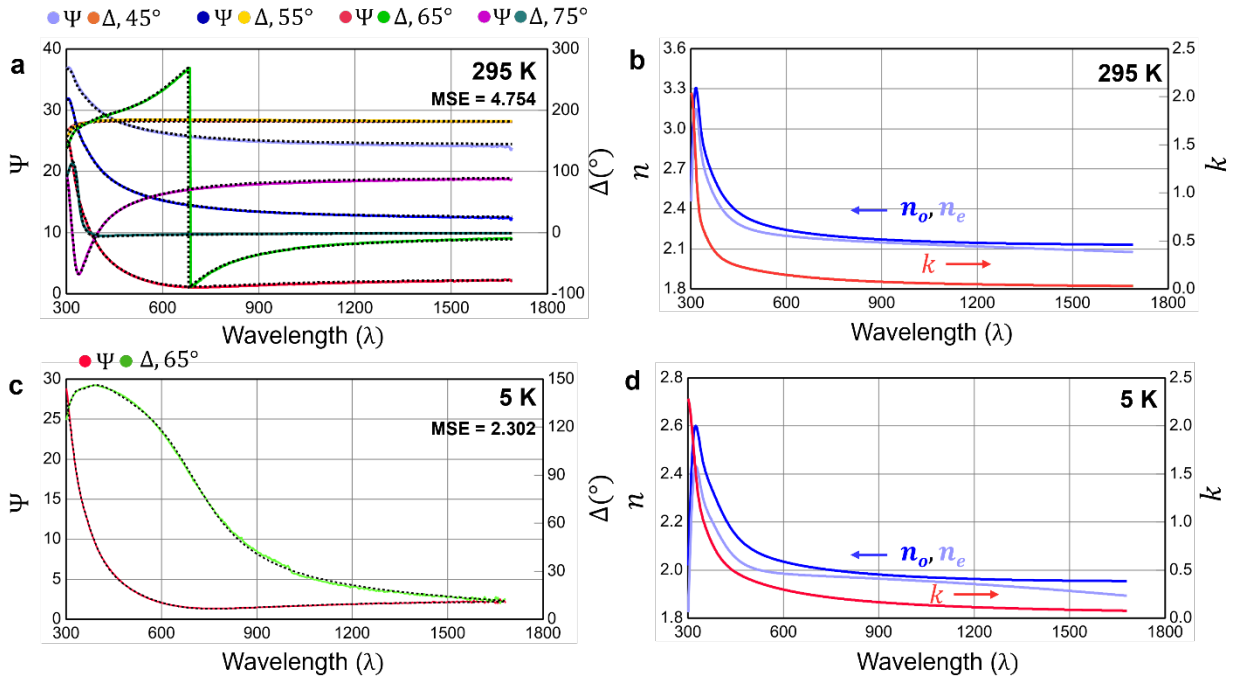


Figure S9: a) Room temperature Ψ and Δ parameters collected at 45°, 55°, 65° and 75° incidence angles from 300 nm to 1689 nm wavelength range fitted to an anisotropic Gaussian Oscillator model. **b)** Derived spectroscopic complex refractive indices of $KNbO_3$ grown on $GdScO_3$ substrate at 295 K. **c)** 5 K Ψ and Δ parameters collected at 65° incidence angle from 300 nm to 1689 nm wavelength range fitted to a anisotropic Gaussian Oscillator model. **d)** Derived spectroscopic complex refractive indices of $KNbO_3$ grown on $GdScO_3$ substrate at 5 K.

Temperature dependent linear optical properties of $KNbO_3$ on $GdScO_3$ was measured using a J. A. Woollam M-2000XI rotating-compensator, variable angle spectroscopic ellipsometer. Ψ and Δ parameters were collected at 45°, 55°, 65° and 75° incidence angles from 300 nm to 1689 nm wavelength range. To extract complex refractive index, $n + ik$, the spectra was fitted using a least-squares regression analysis of a semi-infinite $GdScO_3$ substrate and a finitely thick $KNbO_3$ film.

Firstly, measurements were performed on a bare $GdScO_3$ substrate, which was fitted to a Cauchy oscillator-based dielectric model; $n(\lambda) = A + \frac{B}{\lambda^2} + \frac{C}{\lambda^4}$, where λ represents wavelength in units of μm. The model also includes an Urbach absorption tail to account for the imaginary component of the refractive index, k, where $k = k_{amp}\, e^{G(E-E_g)}$. In the Urbach tail equation, k_{amp} and E_g are coupled variables during fitting, and hence E_g does not have a unique solution. Fit parameters obtained for the $GdScO_3$ substrate are: $A = 2.000$, $B = 0.01186$, $C = 0.00044261, k_{amp} = 0.23967, G = 0.475$. This substrate layer was assumed fixed for subsequent modeling of $KNbO_3$ film on $GdScO_3$.

To model the $KNbO_3$ film a Gaussian oscillator based dielectric model was used to fit the ellipsometry spectra. The form of the Gaussian oscillators is given by $\varepsilon_{Gaussian_i} = Amp_i\left\{\left[\Gamma\left(\frac{E-En_i}{\sigma_i}\right)+\Gamma\left(\frac{E+En_i}{\sigma_i}\right)\right]+i\cdot\left(\exp\left[-\left(\frac{E-En_i}{\sigma_i}\right)^2\right]-\exp\left[-\left(\frac{E+En_i}{\sigma_i}\right)^2\right]\right)\right\}$, where $\sigma_i = \frac{Br_i}{2\sqrt{\ln(2)}}$ and Γ is a convergence series that produces a Kramers-Kronig consistent line shape for $\varepsilon_{Gaussian_i}$.[7,8] The real part of the dielectric function is further affected by a wavelength-independent constant, ε_∞, along with UV and IR poles that account for resonances further away from the measurement spectral range: $\varepsilon_{IR} = \frac{Amp_{IR}}{En_{IR}^2-E^2}$ and $\varepsilon_{UV} = \frac{Amp_{UV}}{En_{UV}^2-E^2}$.

An initial isotropic model accounting for the ordinary refractive index, n_o, of $KNbO_3$ was assumed to fit the room temperature ellipsometry spectra of $KNbO_3$ on $GdScO_3$ measured at 45° incidence angle. An initial guess of 19 nm for the film thickness was assumed based on x-ray reflectivity measurements. This was then used to create an identical model for the extraordinary refractive index, n_e, by defining the $KNbO_3$ layer as anisotropic, with the extraordinary axis oriented in the out-of-plane direction. The extraordinary index is determined by summing the ordinary optical constants with "difference" values calculated from an extended Cauchy dispersion equation: $d\varepsilon_i$.[9] The difference parameters serve as fitting parameters for the extraordinary index and are subsequently, unconstrainted and allowed to converge to fit the 75° incidence angle data, with the ordinary optical constants fixed. Both n_o and n_e optical parameters were then unconstrainted and allowed to converge to simultaneously fit the ellipsometry spectra measured at 45°, 55°, 65° and 75° incidence – giving the final birefringent model for the refractive indices. Finally, the film thickness was unconstrainted along with the n_o and n_e oscillator parameters. **Figure S9 a,b** shows the fitted room temperature Ψ and Δ spectra and extracted optical properties at room temperature. The necessary fit parameters are summarized below (**Table S2**):

Table S2: Room temperature fit parameters of $KNbO_3$ on $GdScO_3$

	Oscillator details		
#	Amp_i	Br_i	En_i
1	5.470214	0.2660	4.038
2	1.027880	0.2873	4.626
3	1.593587	3.5956	4.101
4	5.874370	1.3038	4.463

Other associated fit parameters: $t = 20.02$ nm, $\varepsilon_\infty = 6.714$, $Amp_{IR} = 0.0211$, $En_{IR} = 0\ eV$, $Amp_{UV} = 916.891$, $En_{UV} = 10.090\ eV$, $d\varepsilon_A = 0.026060$, $d\varepsilon_B = -0.826523$, $d\varepsilon_C - 0.017993$, $d\varepsilon_D = 0.003074$, $d\varepsilon_{IR} = 1.00000$.

For measuring temperature-dependent refractive index, Oxford Instruments MicrostatHe gas flow cryostat was used with the Woollam M-2000XI ellipsometer. The cryostat windows are aligned

normally to the incident probe beam when measurements are made at 65° incidence angle. This results only in modulation of the ellipsometry probe intensity without affecting Ψ and Δ quantities when data was collected at that angle. As such, Ψ and Δ spectra were collected for an incident angle of 65° between 5 K to 295 K. During the cooling process, the cryostat chamber was pumped to a vacuum of 10^{-5} Torr at room temperature. No sample icing was observed, which would lead to periodic fluctuations in Ψ and Δ with wavelength for ice with few ~100 nanometer thickness on sample. Thus, all changes in Ψ and Δ are attributed to changes in the refractive index of the $KNbO_3$ film. The previously developed room temperature birefringent model is allowed to relax in order to best fit the low temperature data. While a monoclinic structure is expected to be biaxial, the limited geometry within the cryostat reduces the ability to sample the anisotropy of the sample. Furthermore, with 4 domain variants expected and a large probe size of roughly 2x4 mm^2, the observed optical response is expected to sample an average of all domain variants, with the in-plane index a domain average of n_1 and n_2, with the out-of-plane index of n_3 and therefore effectively uniaxial. The fit parameters for the film at 5 K are given in **Table S3** below. **Figure S9 c,d** show the fitted room temperature Ψ and Δ spectra and extracted optical properties at room temperature. The temperature dependence of the linear optical properties of $KNbO_3$ on $GdScO_3$ at 1550 nm is shown in **Figure S10a**.

Table S3: 5 K fit parameters of $KNbO_3$ on $GdScO_3$

	Oscillator details		
#	Amp_i	Br_i	En_i
1	5.470214	0.2660	4.038
2	1.027880	0.2873	4.626
3	1.593587	3.5956	4.101
4	5.874370	1.3038	4.463

Other associated fit parameters: $t = 20.02$ nm, $\varepsilon_\infty = 6.714$, $Amp_{IR} = 0.0211$, $En_{IR} = 0\ eV$, $Amp_{UV} = 916.891$, $En_{UV} = 10.090\ eV$, $d\varepsilon_A = 0.026060$, $d\varepsilon_B = -0.826523$, $d\varepsilon_C - 0.017993$, $d\varepsilon_D = 0.003074$, $d\varepsilon_{IR} = 1.00000$.

Since the beam size used in our experiments are averaging across all domains, our measurements for the monoclinic phase assume the sample as effectively uniaxially with two refractive indices: out-of-plane refractive index n_e and in-plane refractive index n_o. Using the formalism described in **Note 2**, $n_e(\theta_{film})$ can be calculated as a function of temperature assuming the 45° incidence angle used in electro-optic measurements (**Figure S10b**).

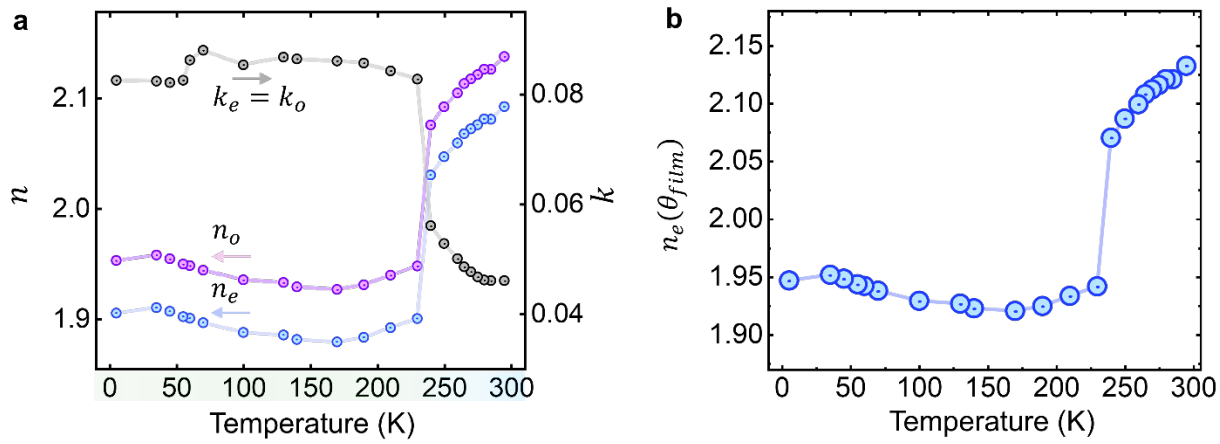


Figure S10: a) Temperature-dependence of ordinary and extra-ordinary linear optical properties of $KNbO_3$ on $GdScO_3$ at 1550 nm measured by spectroscopic ellipsometry n_e represents the extraordinary refractive index (out-of-plane) and n_o represents the ordinary refractive index (in-plane). Our measurements are not sensitive to in-plane anisotropy of the monoclinic phase since the beam size used in our experiments averages over many domains (domain periodicity ~30nm). Hence, for the monoclinic phase the sample is treated as effectively uniaxial. **b)** The formalism proposed in **Note 2** is used assuming a probe incidence angle of 45° used for electro-optic measurements.

UV-Vis spectroscopy:

Overestimation of k-values of thin films through ellipsometry is well known[30,31]. Hence, to accurately determine the extinction coefficient of the $KNbO_3$ film and the $GdScO_3$ substrate, we performed additional UV-Vis transmission measurements on a 0.7 mm thick $GdScO_3$ reference substrate and a 30 nm $KNbO_3$ thin film grown on $GdScO_3$ (**Figure S11a**).

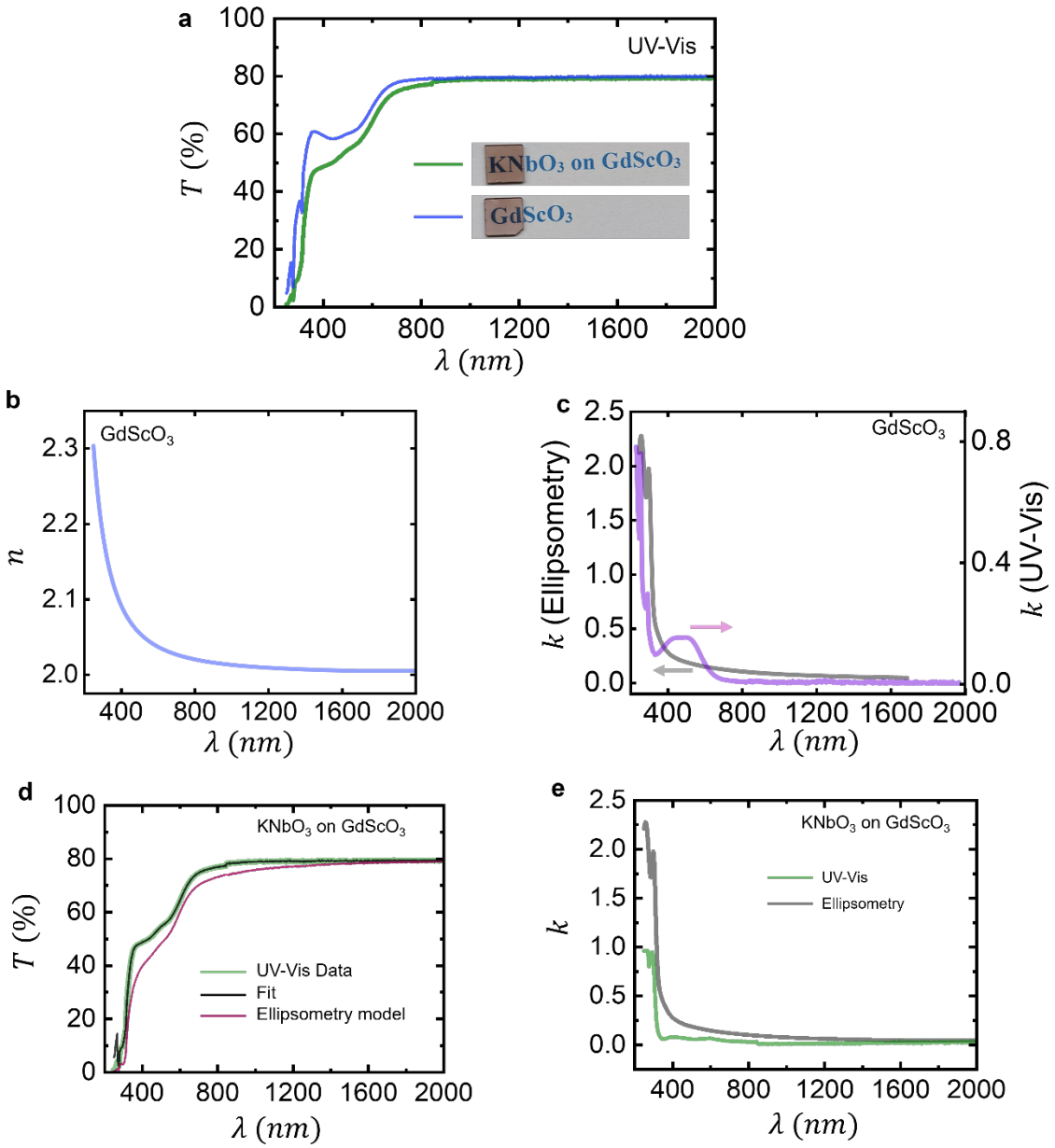


Figure S11: **a)** Transmission UV-Vis spectra of $KNbO_3$ on $GdScO_3$ substrate compared to a bare $GdScO_3$ substrate for reference. Inset shows image of the two samples. The orange tint of the $GdScO_3$ substrate arise from excess Gd in the substrate. **b)** Refractive index (n) of $GdScO_3$ measured from ellipsometry. **c)** Comparison between k-values extracted from ellipsometry and UV-Vis. **d)** UV-Vis spectra of $KNbO_3$ on $GdScO_3$ (green) modeled with a multi-reflection model (black). This is compared to forward simulated UV-Vis spectra using n and k values extracted from ellipsometry. **e)** Comparison between k-values extracted from ellipsometry and UV-Vis.

To accurately determine the k-values of the substrate, the measured transmission was analyzed using a thick-slab model accounting for multiple reflections. The transmission through the substrate, T_s, can be expressed as:

$$T_{\mathrm{s}} = \frac{(1-R)^2 e^{-\alpha d}}{1-R^2 e^{-2\alpha d}}$$

where, $R = \frac{(n_s-1)^2+k_s^2}{(n_s+1)^2+k_s^2}$, absorption coefficient, $\alpha = \frac{4\pi k_s}{\lambda}$, and $d = 0.7\ mm$ is the thickness of the substrate. This is used to model the UV-Vis transmission data from the substrate. For modeling, the n_s-values (refractive index of $GdScO_3$) is used from ellipsometry measurements (**Figure S11b**), while k_s-values is allowed to relax at each wavelength. **Figure S11c** shows the extracted extinction coefficient, k_s, from UV-Vis compared to ellipsometry. The substrate extinction coefficient is $\sim 10^{-4}$ across the visible and near-infrared, which is orders of magnitude lower than the ellipsometry values consistent with the high measured transmission (~80%) through a 0.7 mm substrate. An ellipsometry k_s of magnitude ~0.016 at 1550 nm applied over the full substrate thickness would render the substrate opaque. A picture of the $GdScO_3$ substrate and the $KNbO_3$ on $GdScO_3$ sample is shown in inset of **Figure S11a**. The orange tint in the $GdScO_3$ substrate arises due to excess Gd in the substrate. Correspondingly, the measured k_s from UV-Vis shows a shoulder peak around 400 to 600 nm (**Figure S11c**).

The extinction coefficient of the $KNbO_3$ film (k_f) was then determined from the measured UV-Vis transmission of the film-on-substrate stack. Using complex refractive indices, $\tilde{n}_0 = 1$ (air), $\tilde{n}_1 = n_f + ik_f$ (film) and $\tilde{n}_2 = n_s + ik_s$ (substrate), the Fresnel coefficients at the air-film interface (01) and the film-substrate interface (02) can be written as:

$$r_{01} = \frac{\tilde{n}_0 - \tilde{n}_1}{\tilde{n}_0 + \tilde{n}_1}, t_{01} = \frac{2\tilde{n}_0}{\tilde{n}_0 + \tilde{n}_1}, r_{12} = \frac{\tilde{n}_1 - \tilde{n}_2}{\tilde{n}_1 + \tilde{n}_2}, t_{12} = \frac{2\tilde{n}_1}{\tilde{n}_1 + \tilde{n}_2}$$

where, r_{01} and t_{01} are the reflection and transmission coefficients at the air-film interface and r_{12} and t_{12} are the reflection and transmission coefficients at the film-substrate interface. Assuming multiple-reflections in the film the transmission coefficient from air to the substrate (t_{012}) can be written as:

$$t_{012} = \frac{t_{01} t_{12} e^{i\beta}}{1 + r_{01} r_{12} e^{2i\beta}}$$

where, $\beta = 2\pi\tilde{n}_1 d_f/\lambda$ and $d_f = 30\ nm$.

This gives the intensity transmittance from air into the substrate, T_{fs}, expressed as:

$$T_{\mathrm{fs}} = n_s \mid t_{012} \mid^2$$

This light then propagates through the thick substrate. The substrate bulk transmission, $T_a = \exp(-4\pi k_s d_s/\lambda)$, the substrate/air (23) interface reflectance $R_{23} = \frac{(n_s-1)^2+k_s^2}{(n_s+1)^2+k_s^2}$, transmittance

$T_{23} = 1 - R_{23}$, and substrate/film interface (21) reflectance, $R_{21} = \left|\frac{r_{21}+r_{10}e^{2i\beta}}{1+r_{21}r_{10}e^{2i\beta}}\right|^2$ are considered in the model. Including multiple reflections within the substrate, the net transmission through the film-substrate stack can then be written as:

$$T_{\text{net}} = \frac{T_{\text{fs}}T_a T_{23}}{1 - R_{21}R_{23}T_a^2}$$

The measured UV-Vis transmission through the $KNbO_3$ on $GdScO_3$ sample is then modeled (**Figure S11d**) with the above equation, where the refractive indices of the film and substrate are taken from ellipsometry measurements and extinction coefficient of the substrate is taken from substrate UV-Vis measurements as shown in **Figure S11c**. The extracted extinction coefficients of the film (k_f) is shown in **Figure S11e**, as compared to ellipsometry k-values.

Additionally, forward simulation of the UV-Vis spectra from ellipsometry derived n and k-values are performed, as shown in **Figure S11d** (red curve). The ellipsometry simulated UV-Vis spectra shows lower transmission as compared to the experimentally measured signal, further confirming the overestimation of k-values in ellipsometry.

The extracted linear optical properties of $KNbO_3$ are shown in **Figure 5b, Main Text**.

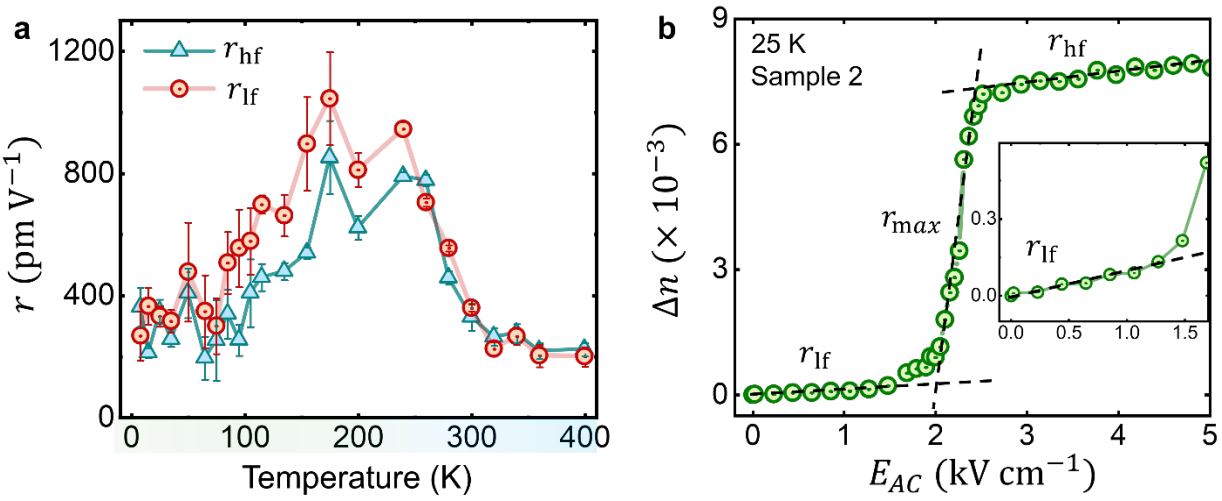


Figure S12: a) Comparison of experimentally measured temperature evolution of r_{lf} and r_{hf}. **b)** Multi-regime Δn vs E_{AC} curves reproduced on a second $KNbO_3$ on $GdScO_3$ sample with coefficients $r_{\mathrm{lf}} = 223 \pm 24$ pm V^{-1}, $r_{\mathrm{max}} = 40{,}416 \pm 3{,}533$ pm V^{-1}, and $r_{\mathrm{hf}} = 625 \pm 94$ pm V^{-1}. The measurement was done at a modulation frequency of 555 Hz at 25 K. Inset shows zoomed in low-field regime.

Note 7: Tensor nature of the observed electro-optic response

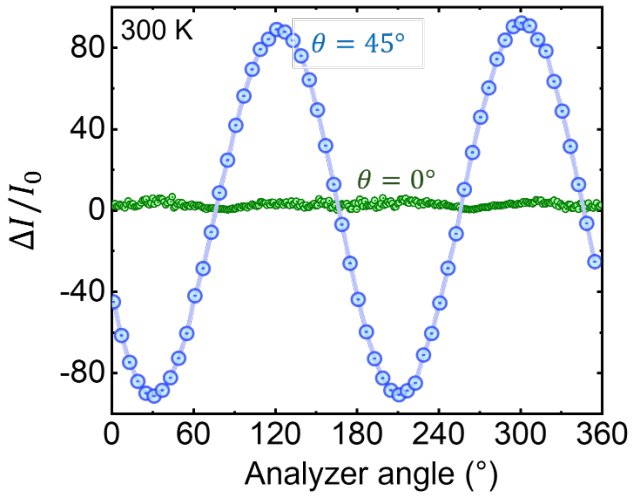


Figure S13: a) 300 K modulated analyzer sweeps normalized to the maximum unmodulated signal ($\Delta I/I_0$) measured at oblique incidence ($\theta = 45°$) and normal incidence ($\theta = 0°$). No electro-optic response is measured at normal incidence at 300 K.

For the room temperature tetragonal phase of $KNbO_3$ films the [001] direction lies in the out-of-plane direction with the in-plane applied electric field would be along the [100] direction. The [001] and [100] directions are the crystal physics 3 and 1 directions respectively. Under an applied electric field E_1 along the crystal physics 1 direction the index ellipsoid of the sample is modified as following:

$$\frac{x^2}{n_1^2} + \frac{y^2}{n_2^2} + \frac{z^2}{n_3^2} + r_{31}E_1z^2 + 2xz\, r_{51}E_1 = 1 \tag{9}$$

At normal incidence, the probe beam will sample the xy-plane of the index ellipsoid which can be described by setting $z = 0$ in equation 2. Since $n_1 = n_2 = n_o$, regardless of the magnitude of E_1 equation 9 reduces to a circle dictated by $\frac{x^2}{n_o^2} + \frac{y^2}{n_o^2} = 1$. Hence, no electro-optic response is measurable at normal incidence (**Figure S13**). As a result, the film is rotated by 45° in the path of the probe as illustrated by **Figure S5a**, with the measured electro-optic response attributable to the r_{51} tensor component.

In the monoclinic phase the crystal physics axes remain unchanged, while additional electro-optic tensor coefficients are involved. For monoclinic symmetry (point group m) with an electric field along the crystal physics 1 direction, r_{11}, r_{21}, r_{31} and r_{51} are the relevant tensor coefficients. The index ellipsoid is modified according to:

$$\frac{x^2}{n_1^2} + r_{11}E_1x^2 + \frac{y^2}{n_2^2} + r_{21}E_1y^2 + \frac{z^2}{n_3^2} + r_{31}E_1z^2 + 2xz\, r_{51}E_1 = 1 \tag{10}$$

In normal incidence, the probe beam samples the xy-plane of the index ellipsoid where **equation 10**, reduced to:

$$\frac{x^2}{n_1^2} + r_{11}E_1x^2 + \frac{y^2}{n_2^2} + r_{21}E_1y^2 \ = 1 \tag{11}$$

As a result, at normal incidence the probe beam at normal incidence measures contributions from both r_{11} and r_{21}. Additional constraints arise due to the multi-domain nature of the thin films as SHG modelling, synchrotron x-ray diffraction (see **Note 1**) and phase-field simulations (**Figure 3, Main Text**). While microstructure is poled along the crystal physics 1 direction, equal volume fractions of unit cells are poled along the crystal 2 and -2 directions. As a result, the r_{21} electro-optic coefficient cancels when averaged across the entire microstructure. Hence, under normal incidence electro-optic measurements, the probe is considered to sample the r_{11} electro-optic coefficient.

Figure S14 shows phase-field simulated r_{11}, r_{31} and r_{51} electro-optic coefficients both under low-field and switching-field regimes. At 5 K, the ratio of r_{51} and r_{31} is ~ 35:1 at low field and 24:1 at the switching field. Hence, the observed electro-optic response is attributed to be dominated by r_{51}.

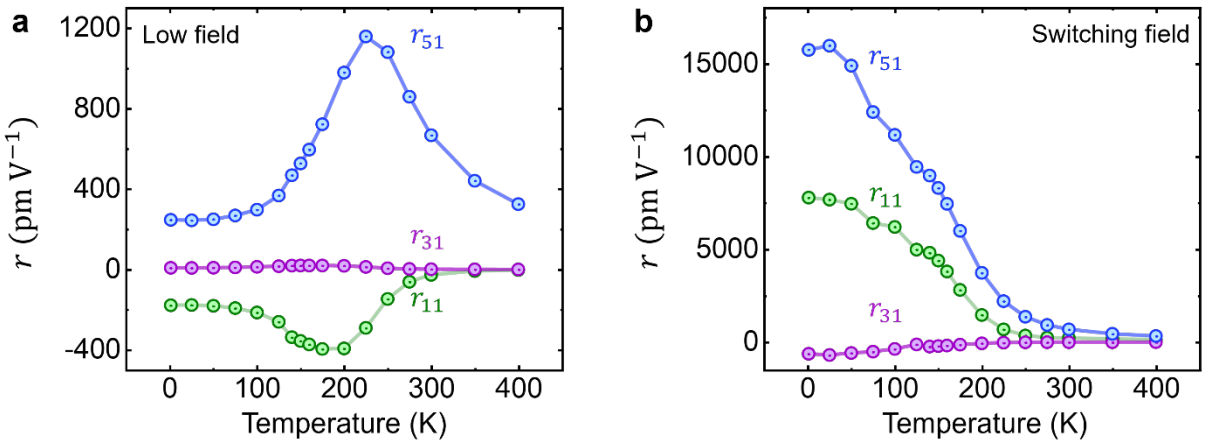


Figure S14: a) Phase-field simulated electro-optic tensor coefficients at low-field. **b)** Phase-field simulated electro-optic tensor coefficients measured at switching field.

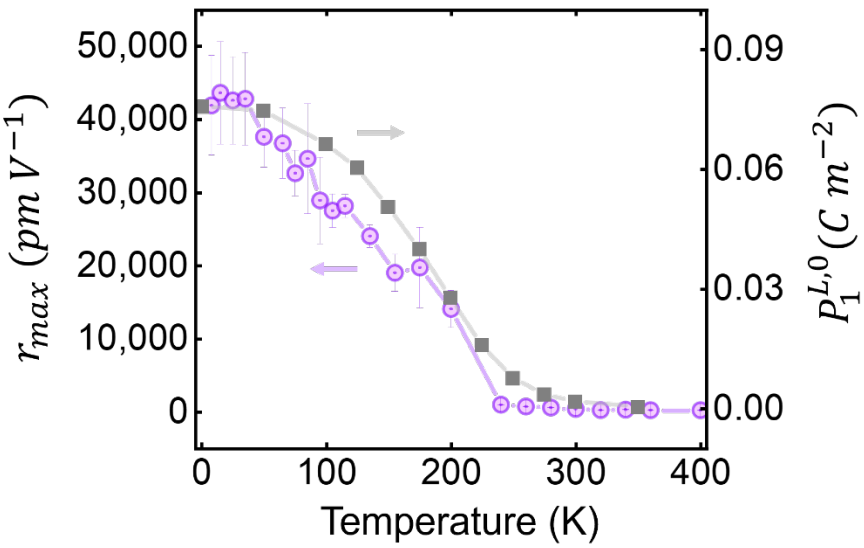


Figure S15: Phase-field simulated in-plane polarization ($P_1^{L,0}$) and switching driven electro-optic response (r_{max}) showing r_{max} increases as $P_1^{L,0}$ increases.

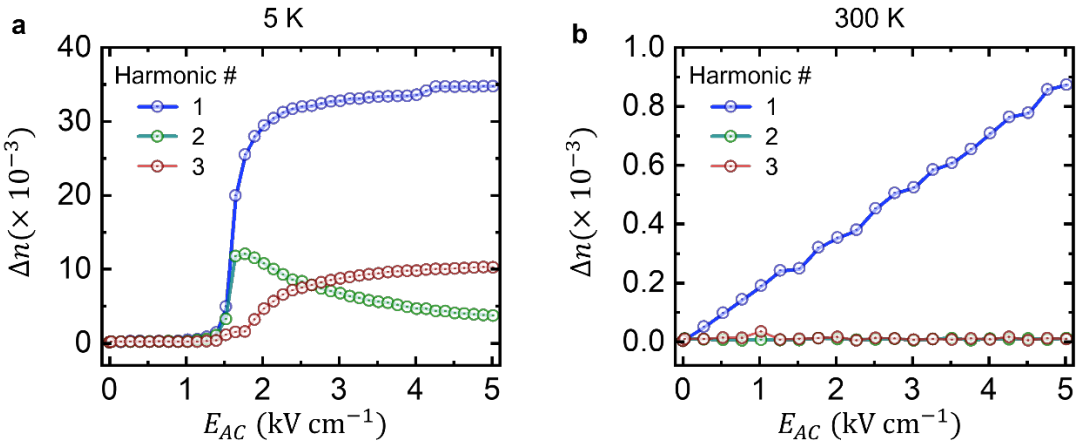


Figure S16: a) 1st, 2nd and 3rd harmonic electro-optic response of $KNbO_3$ measured at 5 K. **b)** 1st, 2nd and 3rd harmonic electro-optic response of $KNbO_3$ measured at 300 K, showing no higher-harmonic response in the tetragonal phase at 300 K.

Note 8: Phase-field simulated effective electro-optic coefficient

The phase-field simulations yield the full electro-optic (EO) tensor coefficients r_{11}, r_{31}, and r_{51} (in Voigt notation) relevant under an applied electric-field in the crystal physics 1 direction. In the experimental geometry, the measured quantity is an effective EO coefficient r_{eff} that depends on the crystal orientation, the beam propagation direction, and the applied field direction. This section describes the numerical procedure used to extract r_{eff} from the phase-field tensor components, implemented in Mathematica.

An electric field E_1 is applied along the crystal physics 1 direction. The EO effect modifies the indicatrix tensor by

$$\Delta B_{ij} = r_{ijk} E_k$$

For a field along *x* and the tetragonal/orthorhombic symmetry of $KNbO_3$, the non-zero increments are:

$$\Delta B_{11} = r_{111} E_1,$$
$$\Delta B_{33} = r_{331} E_1,$$
$$\Delta B_{13} = r_{131} E_1.$$

The full modified optical indicatrix tensor $B' = B + \Delta B$ is constructed from this and using the description presented in **Note 2**, n_o' and $n_e'(\theta_{film})$ is calculated using a applied field of $E_1 = 0.1\ kV\ cm^{-1}$.

As discussed previously in **Note 2**, because the applied field E_1 and the wave vector $\vec{k}$ both lie in the xz-plane, the ordinary polarization (along y) is decoupled from the electro-optic perturbation in this geometry. Consequently, $n_o' = n_o$, while only the extraordinary index changes: $\Delta n_e(\theta_{film}) \neq 0$. This is also confirmed numerically in the simulation (see **Supporting video 1**).

The effective EO coefficient is defined through the standard relation between the field-induced index change and the zero-field extraordinary index:

$$\Delta n = -\tfrac{1}{2}\, r_{\text{eff}}\, n_e^3(\theta_{film}) E_1$$

Rearranging,

$$r_{\text{eff}} = -2\,\Delta n \,/\, [n_e^3(\theta_{film})\, E_1]$$

where $\Delta n_e(\theta_{film}) = n_e(\theta_{film}) - n_e'(\theta_{film})$ and E_1 is the applied field magnitude.

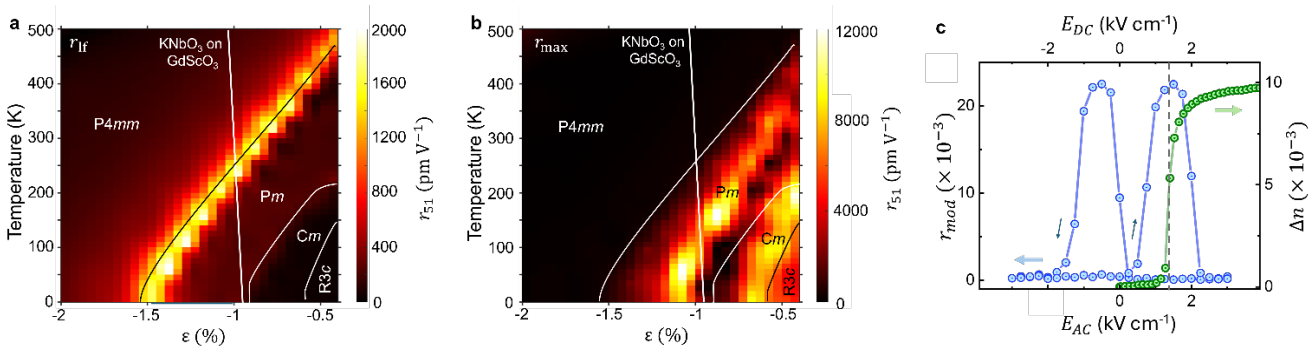


Figure S17: a) Heat map of the phase-field simulated r_{lf} corresponding to the phase diagram of compressively strained $KNbO_3$. **b)** Heat map of the phase-field simulated r_{max} corresponding to the phase diagram of compressively strained $KNbO_3$. Since the experimentally observed electro-optic response is dominated by the r_{51} electro-optic tensor, both r_{lf} and r_{max} heat maps are constructed using r_{51} at low-field and swaying field. **c)** Comparison of the electro-optic hysteresis (r_{mod} vs E_{DC}) and Δn vs E_{AC} curves, both measured at 5 K. The inflection of the Δn vs. E_{AC} curve occurs at maxima of the electro-optic hysteresis curve.

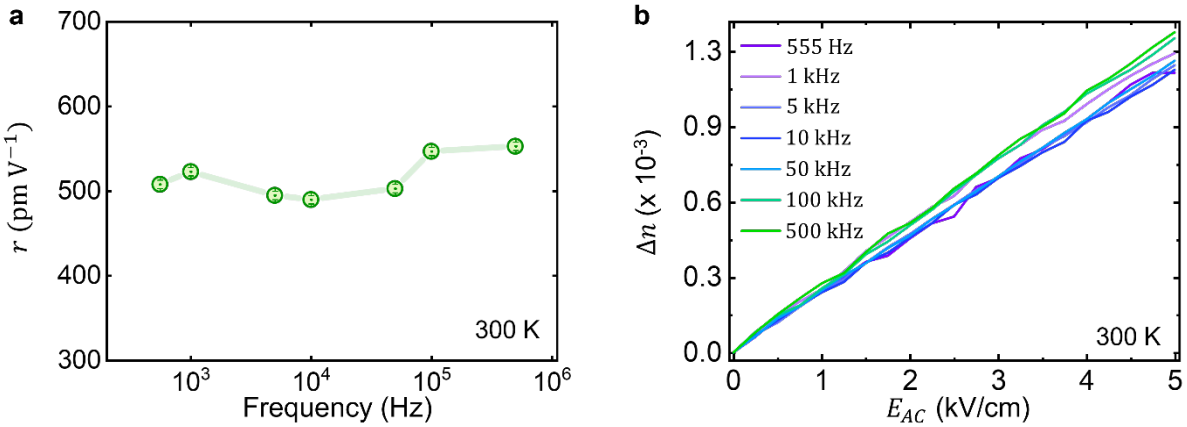


Figure S18: a) Electro-optic coefficient (r_{lf}) at 300 K (tetragonal phase) measured from 555 Hz to 0.5 MHz. **b)** Experimentally measured Δn vs. E_{AC} curves measured at 300 K.

Note 9: Stability of electro-optic response

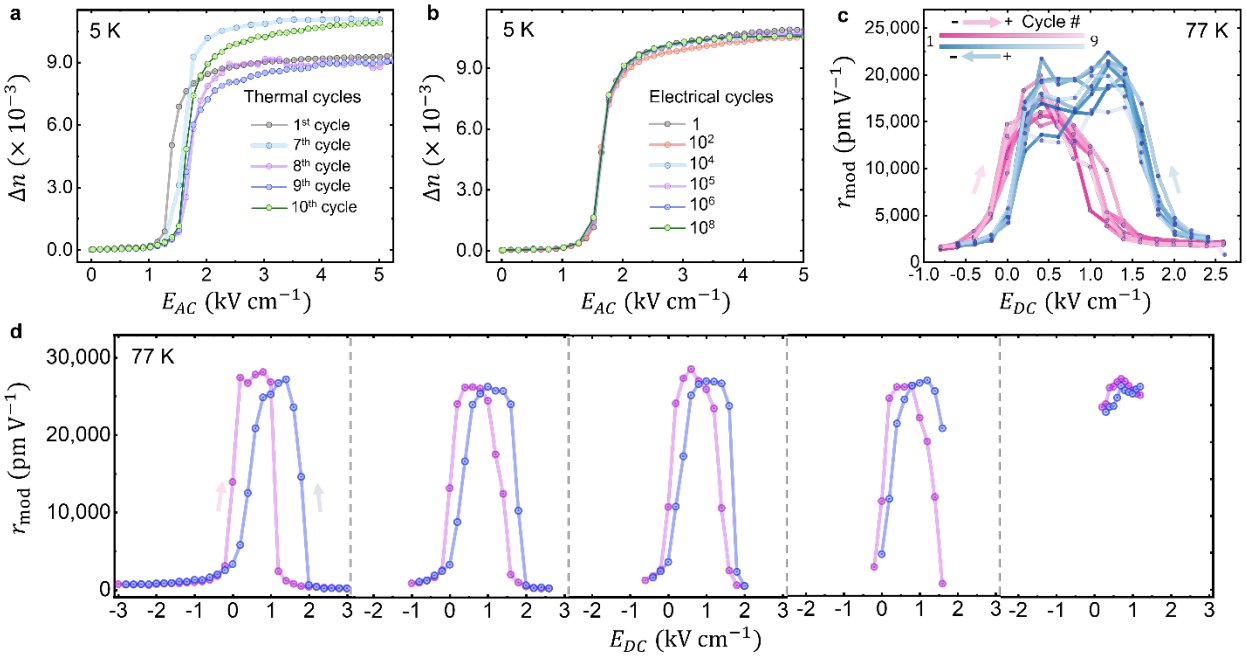


Figure S19: a) Δn vs. E_{AC} curves measured at 5 K after thermally cycling the sample. Before each measurement the sample was heated to 300 K and then cooled back to 5 K. **Table S4** shows the extracted electro-optic coefficients. **b,** Δn vs. E_{AC} curves measured at 5 K after electrically cycling the sample. Before each measurement the sample was electrically cycled using a sine wave with an amplitude of 5 kV cm^{-1} for several times indicated by the legend. **Table S5** shows the extracted electro-optic coefficients. **c**, Reproducibility of r_{mod} obtained through electro-optic hysteresis performed at 77 K measured with a fixed $E_{AC} = 1.25$ kV cm^{-1}. **d)** Reproducibility of r_{mod} measured at 77 K by varying the range of the E_{DC} field sweep window of the electro-optic hysteresis measurements.

Table S4: Electro-optic coefficients with thermal cycling measured at 555 Hz

Thermal cycle #	r_{lf} (pm V^{-1})	$r_{\max}$ (pm V^{-1})	r_{hf} (pm V^{-1})
1	365 ± 36	$43{,}543 \pm 6{,}998$	342 ± 14
7	166 ± 38	$47286 \pm 10{,}628$	175 ± 80
8	144 ± 20	$39{,}013 \pm 5{,}725$	163 ± 104
9	157 ± 18	$37{,}214 \pm 4{,}899$	590 ± 39
10	170 ± 20	$46{,}409 \pm 6123$	877 ± 50

Table S5: Electro-optic coefficients with electrical cycling. Each curve is measured after with an AC frequency of 555 Hz after electrically cycling.

# of electrical cycles applied before measurement	r_{lf} (pm V^{-1})	$r_{\max}$ (pm V^{-1})	r_{hf} (pm V^{-1})
1	170 ± 20	$40{,}098 \pm 5{,}417$	841 ± 45
10^2	157 ± 21	$38{,}055 \pm 5166$	793 ± 60
10^4	228 ± 90	$39{,}773 \pm 13{,}976$	424 ± 71
10^5	151 ± 22	$40{,}692 \pm 14{,}222$	643 ± 106
10^6	166 ± 32	$39{,}773 \pm 14{,}046$	464 ± 56
10^8	164 ± 28	$39{,}896 \pm 14{,}117$	350 ± 72

Note 10: Parameter table for phase-field simulations

Table S6. Coefficients in the thermodynamic free energy function and equation of motion[10]

g_{1111}^{LL}	$27.8 \times 10^{-2}(m^4/C^2)$	p_{1111}	0.5328 (Unitless)
g_{1122}^{LL}	$-1.1 \times 10^{-2}(m^4/C^2)$	p_{1122}	0.1584 (Unitless)
g_{1212}^{LL}	$8.2 \times 10^{-2}(m^4/C^2)$	p_{1212}	-0.432 (Unitless)
a_{11}	$a_o\left(T_s \coth\left(\frac{T_s}{T}\right) - T_s \coth\left(\frac{T_s}{T_c}\right)\right)$	μ_e	$32.8 \times 10^{-23}\left(\frac{Kg}{m}\frac{m^4}{C^2}\right)$
T_c	$650K$	γ_e	$3 \times 10^{-9}\left(\frac{Kg}{ms}\frac{m^4}{C^2}\right)$
T_s	$54K$	$B_{ij}^{e,ref}(T_0)$	0.2546 (Unitless)
a_0	$3.53 \times 10^5\left(\frac{J}{m^3}\ \frac{m^4}{K\,C^2}\right)$	T_0	$398K$
a_{1111}	$-5.86 \times 10^8\left(\frac{J}{m^3}\ \frac{m^8}{C^4}\right)$	α_{11}	$2.657 \times 10^{-5}\left(\frac{1}{K}\right)$
a_{1122}	$9.66 \times 10^8\left(\frac{J}{m^3}\ \frac{m^8}{C^4}\right)$	$a_{11111111}$	$1.74 \times 10^{10}\left(\frac{J}{m^3}\ \frac{m^{16}}{C^8}\right)$
a_{111111}	$2.71 \times 10^9\left(\frac{J}{m^3}\ \frac{m^{12}}{C^6}\right)$	$a_{11111122}$	$5.99 \times 10^9\left(\frac{J}{m^3}\ \frac{m^{16}}{C^8}\right)$
a_{111122}	$-2.2 \times 10^9\left(\frac{J}{m^3}\ \frac{m^{12}}{C^6}\right)$	$a_{11112222}$	$2.5 \times 10^{10}\left(\frac{J}{m^3}\ \frac{m^{16}}{C^8}\right)$
a_{112233}	$4.4 \times 10^9\left(\frac{J}{m^3}\ \frac{m^{12}}{C^6}\right)$	$a_{11112233}$	$-1.63 \times 10^{10}\left(\frac{J}{m^3}\ \frac{m^{16}}{C^8}\right)$
Q_{1111}	$0.11\left(\frac{m^4}{C^2}\right)$	Q_{1122}	$-0.053\left(\frac{m^4}{C^2}\right)$
Q_{1212}	$0.026\left(\frac{m^4}{C^2}\right)$		

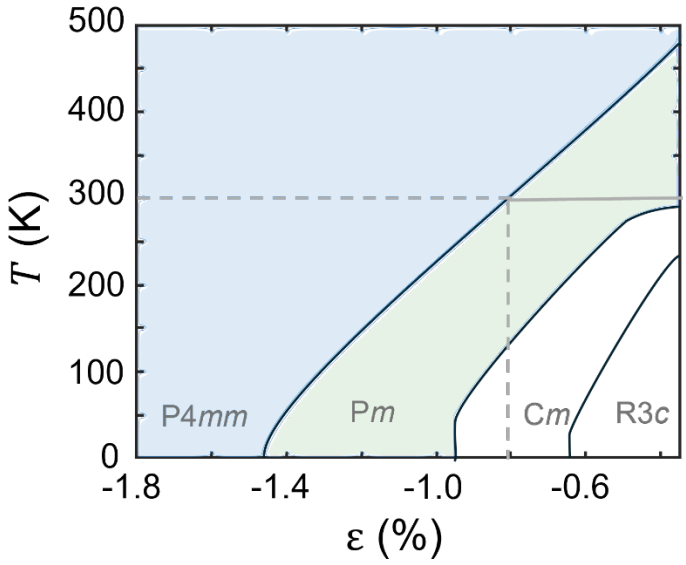


Figure S20: Phase-field simulated phase diagram of $KNbO_3$ in the compressive strained regime. The solid grey line indicates the compressively strained regime ($|\varepsilon| < 0.8\%$) where a monoclinic phase can be established at room temperature.

Variable	Value (units)
$n_{11} = n_{22}$ (5 K) of $KNbO_3$	1.9530
n_{33} $(5K)$ of $KNbO_3$	1.9054
n of GdScO3 (isotropic)	2.07
n of SiO2 (isotropic)	1.4
n of Si	3.48
Thickness of KNbO3 layer	100 nm
Thickness of silicon layer	100 nm
Width of silicon layer	0.7 μm
Wavelength	1550 nm

Table S7: Parameters used for COMSOL simulations.

References

[1] S. Hazra, T. Schwaigert, A. Ross, H. Lu, U. Saha, V. Trinquet, B. Akkopru-Akgun, B. Z. Gregory, A. Mangu, S. Sarker, T. Kuznetsova, S. Sarker, X. Li, M. R. Barone, X. Xu, J. W. Freeland, R. Engel-Herbert, A. M. Lindenberg, A. Singer, S. Trolier-McKinstry, D. A. Muller, G. Rignanese, S. Salmani-Rezaie, V. A. Stoica, A. Gruverman, L. Chen, D. G. Schlom, V. Gopalan, *Advanced Materials* **2024**, DOI 10.1002/adma.202408664.

[2] S. A. Denev, T. T. A. Lummen, E. Barnes, A. Kumar, V. Gopalan, *Journal of the American Ceramic Society* **2011**, *94*, 2699.

[3] L. Bogula, L. von Helden, C. Richter, M. Hanke, J. Schwarzkopf, M. Schmidbauer, *Nano Futures* **2020**, *4*, 035005.

[4] A. Suceava, S. Hazra, A. Ross, I. R. Philippi, D. Sotir, B. Brower, L. Ding, Y. Zhu, Z. Zhang, H. Sarkar, S. Sarker, Y. Yang, S. Sarker, V. A. Stoica, D. G. Schlom, L. Chen, V. Gopalan, *Advanced Materials* **2026**, *38*, DOI 10.1002/adma.202507564.

[5] S. Abel, T. Stöferle, C. Marchiori, C. Rossel, M. D. Rossell, R. Erni, D. Caimi, M. Sousa, A. Chelnokov, B. J. Offrein, J. Fompeyrine, *Nat. Commun.* **2013**, *4*, 1671.

[6] M. Reynaud, M. Waqar, C. Du, A. B. Posadas, X. Pan, A. A. Demkov, *Commun. Mater.* **2025**, *6*, 176.

[7] D. De Sousa Meneses, M. Malki, P. Echegut, *J. Non. Cryst. Solids* **2006**, *352*, 769.

[8] K.-E. Peiponen, E. M. Vartiainen, *Phys. Rev. B* **1991**, *44*, 8301.

[9] H. Fujiwara, *Spectroscopic Ellipsometry*, Wiley, **2007**.

[10] A. Ross, V. Gopalan, L.-Q. Chen, *ArXiv* **2026**.